INTERNATIONAL ATOMIC ENERGY AGENCY
UNITED NATIONS EDUCATIONAL, SCIENTIFIC AND CULTURAL ORGANIZATION

INTERNATIONAL CENTRE FOR THEORETICAL PHYSICS
34100 TRIESTE (ITALY) - P.O.B. 586 - MIRAMARE - STRADA COSTIERA 11 - TELEPHONE: 2360-1
CABLE: CENTRATOM - TELEX 460392-1

H4.SMR/285 - 39

WINTER COLLEGE ON
LASER PHYSICS: SEMICONDUCTOR LASERS
AND INTEGRATED OPTICS

(22 February - 11 March 1988)

OPTOELECTRONIC INTEGRATED CIRCUITS

F.K.Reinhart
Ecole Polytechnique de Lausanne
Institute de Micro- & Opto Electronics
Lausanne
Switzerland

OPTOELECTRONIC INTEGRATED CIRCUITS

F.K. Reinhart
Institute of Micro- and Optoelectronics
Swiss Federal Institute of Technology
1015 - LAUSANNE
Switzerland

I. INTRODUCTION

II. MATERIAL

- Molecular Beam Epitaxy
- Layers for OEIC
- Quantum Wells
- Superlattices

III. GRATING

- Holographic Fabrication
- Results

IV. WAVEGUIDE

- Modulation
- Loss
- Applications

EPF-LAUSANNE INSTITUT DE MICRO- ET OPTOÉLECTRONIQUE

V. FET FOR OPTICAL INTEGRATION

VI. MONOLITHIC APPROACHES

- Integration Levels
- Electrical Optical Integration
- Optical-Optical Integration
- Examples

Lausanne, March 9, 1988
FKR/mg

INTEGRATED OPTOELECTRONIC CIRCUITS

THE MONOLITHIC INTEGRATION OF ELECTRONIC AND OPTICAL FUNCTIONS ON A SINGLE SEMICONDUCTOR CRYSTAL HAS BECOME KNOWN AS INTEGRATED OPTOELECTRONIC CIRCUITS.

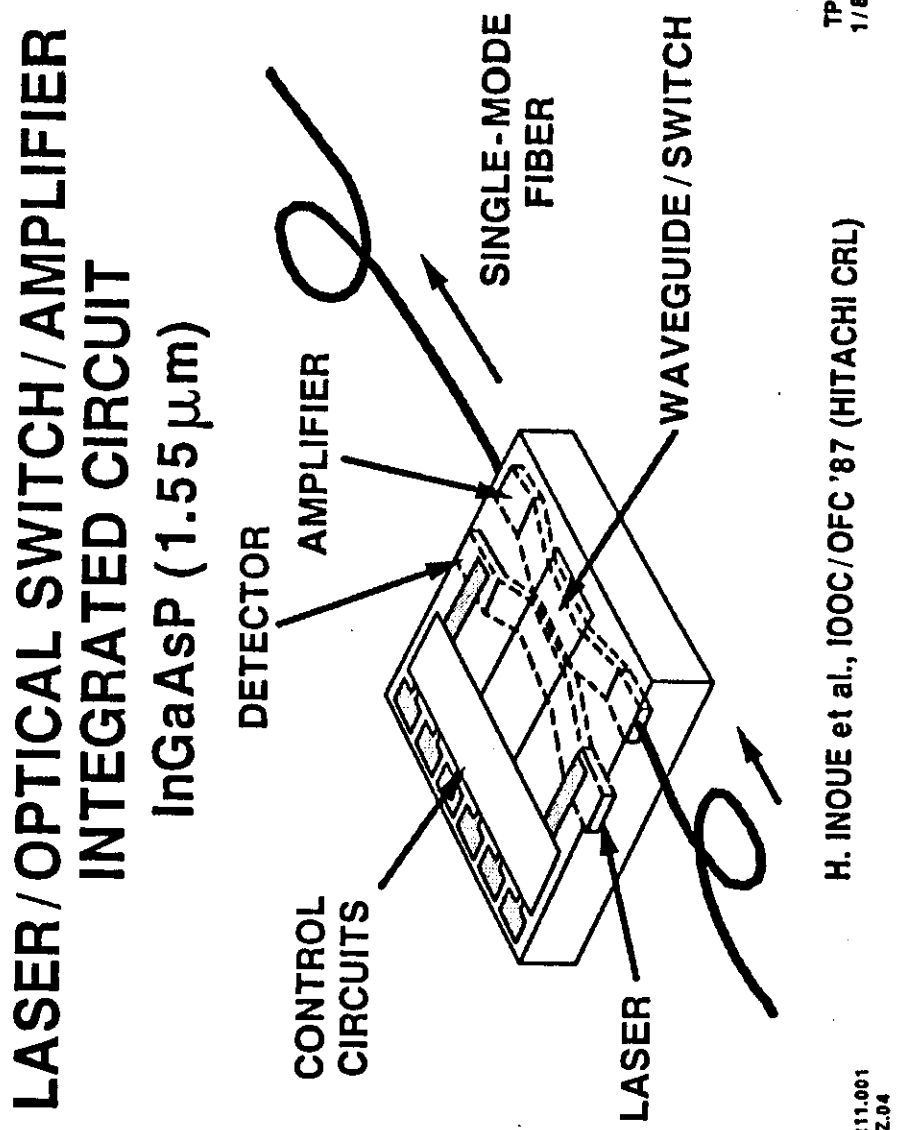

II. MATERIALS

Semiconductors	E_g (eV)	Type	x_c	E_{gc} (eV)	Laser
Si	1,12	I			
Ge	0,67	I			
GaAs	1,42	D			+
$A\ell_xGa_{1-x}As$	1,42-2,17	D-I	0,45	1,985	+
InP	1,35	D			+
$In_{1-x}Ga_xAs$	0,42-1,42	D			+
$In_{1-x}A\ell_xAs$	0,42-2,17	D-I	0,68	2.05	+
InP - $In_{0,53}Ga_{0,47}As$	0,86	D			+
InP - $In_{0,53}A\ell_{0,47}As$	1,46	D			+
$In_{1-x}Ga_xAs_{1-y}P_y$	0,74-1,35	D	x=2,13y		+
$In_{0,53}[Ga_{1-y}A\ell_y]_{0,47}As$	0,80-1,50	D			+

Table I Bandgap of some semiconductors. (D: direct, I: indirect). The critical composition x_c that separates the types D and I, and the corresponding value of the gap, E_{gc}, are also given. The "+" indicates that laser action is possible for $x < x_c$.

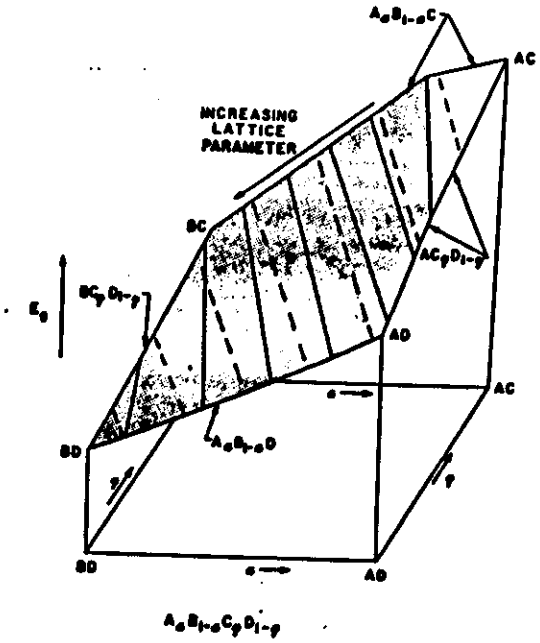

FIG. 1 ENERGY GAP VERSUS COMPOSITION FOR THE QUARTERNARY $A_xB_{1-x}C_yD_{1-y}$. The light dashed lines show isolattice parameter compositions. Th solid lines are isoenergy gap compositions. The shaded area is th direct energy gap region. Note that the corners represent binary compounds and that the sides represent ternary compounds.

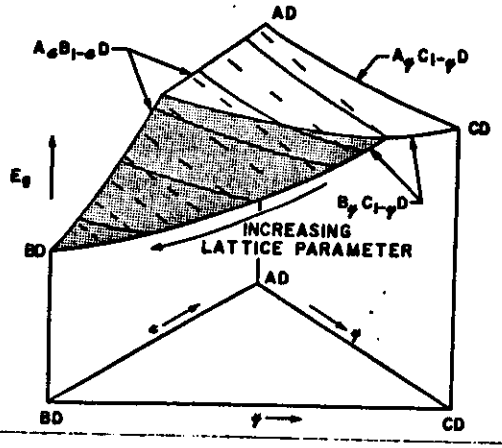

FIG. 2 ENERGY GAP VERSUS COMPOSITION FOR THE QUATERNARY $(A_xB_{1-x})_yC_{1-y}D$. The explanation corresponds to Fig.1

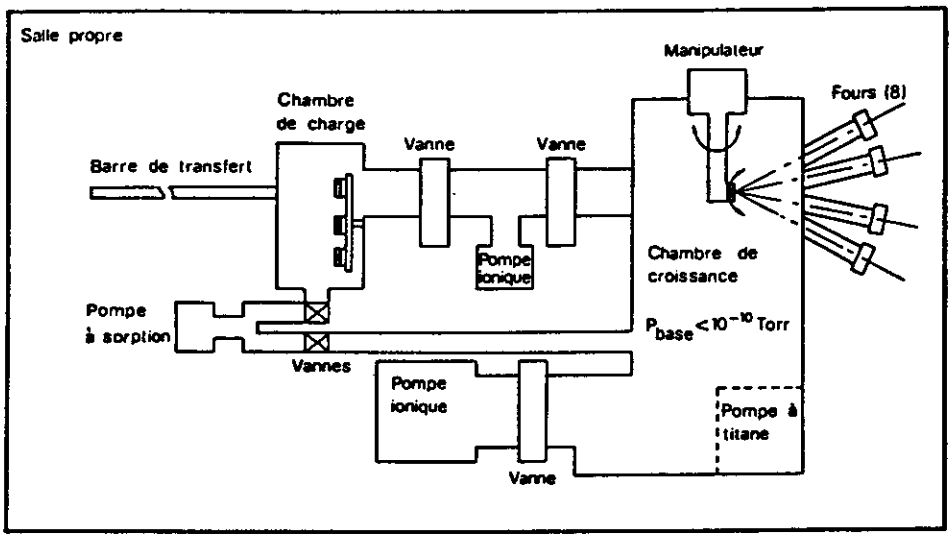

MOLECULAR BEAM EPITAXY

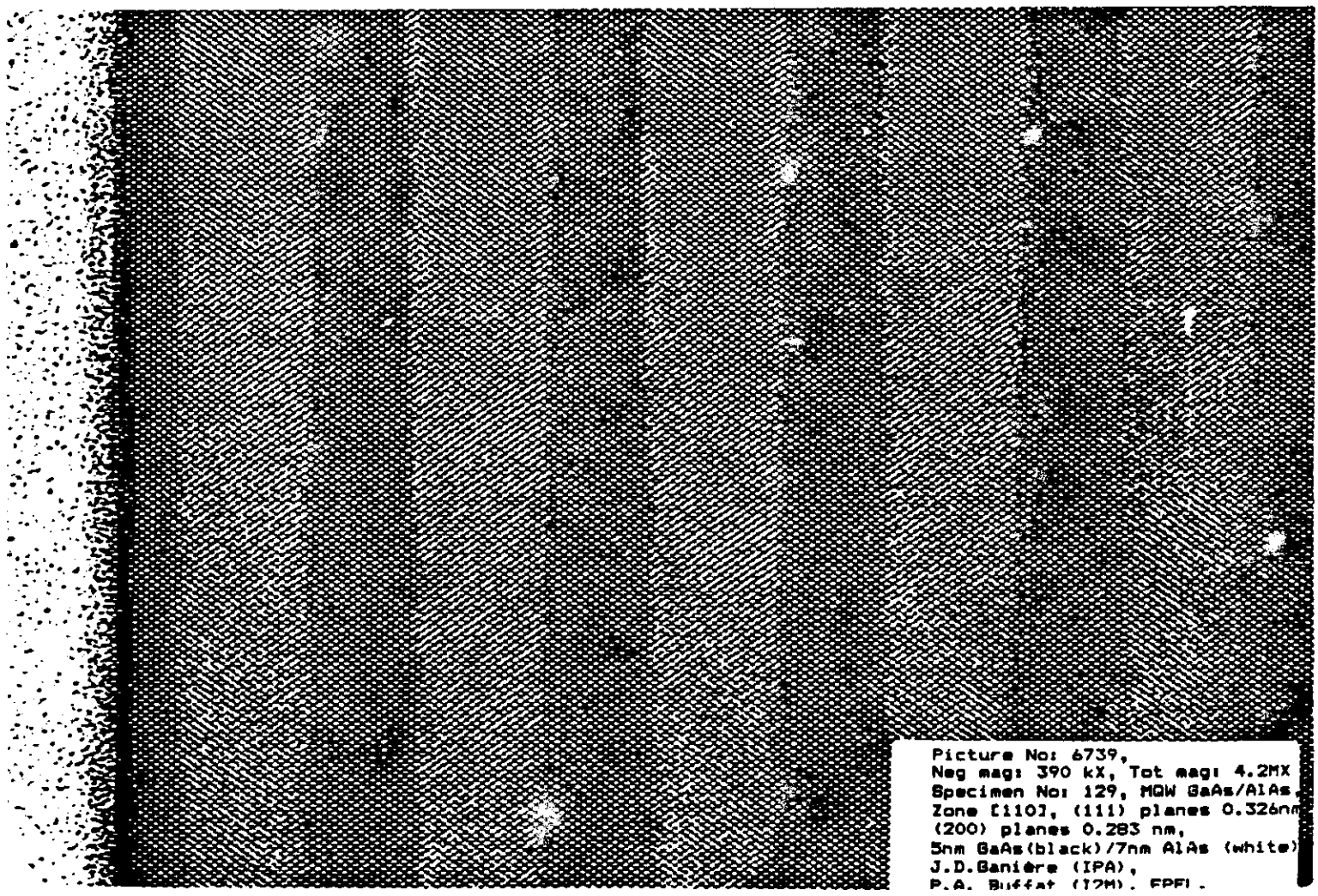

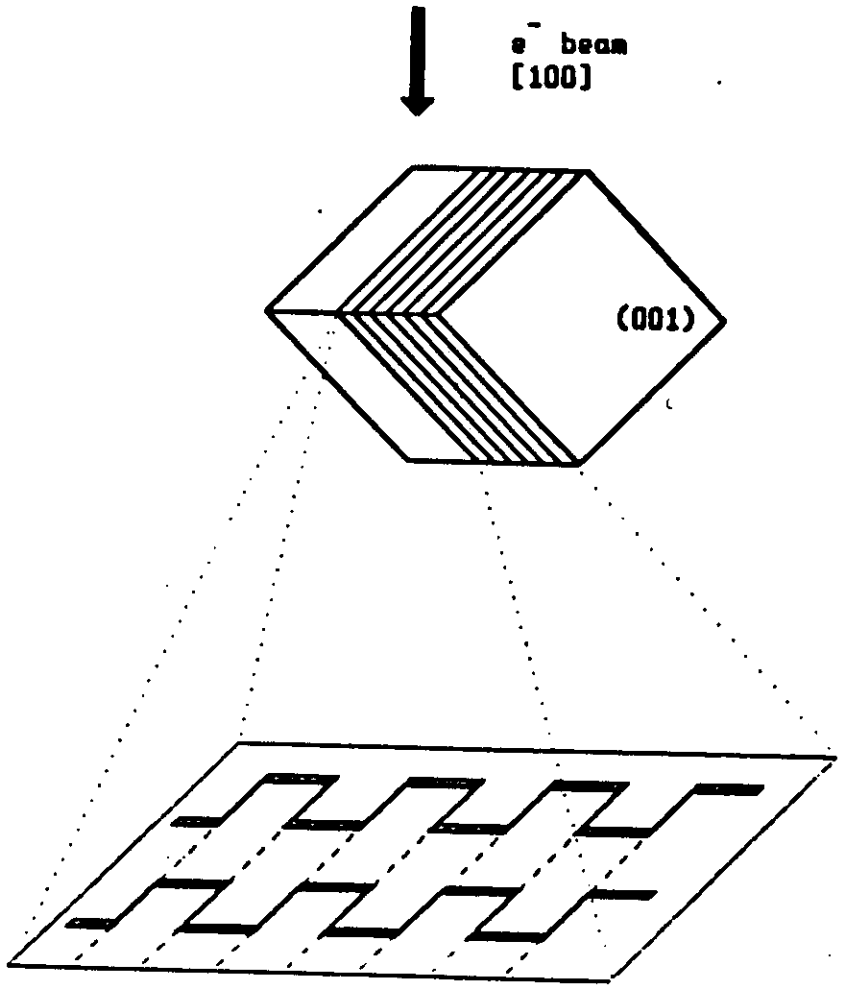

Composition dependance of the equal thickness fringes in an electron microscope image of AlGaAs/GaAs multilayer structure

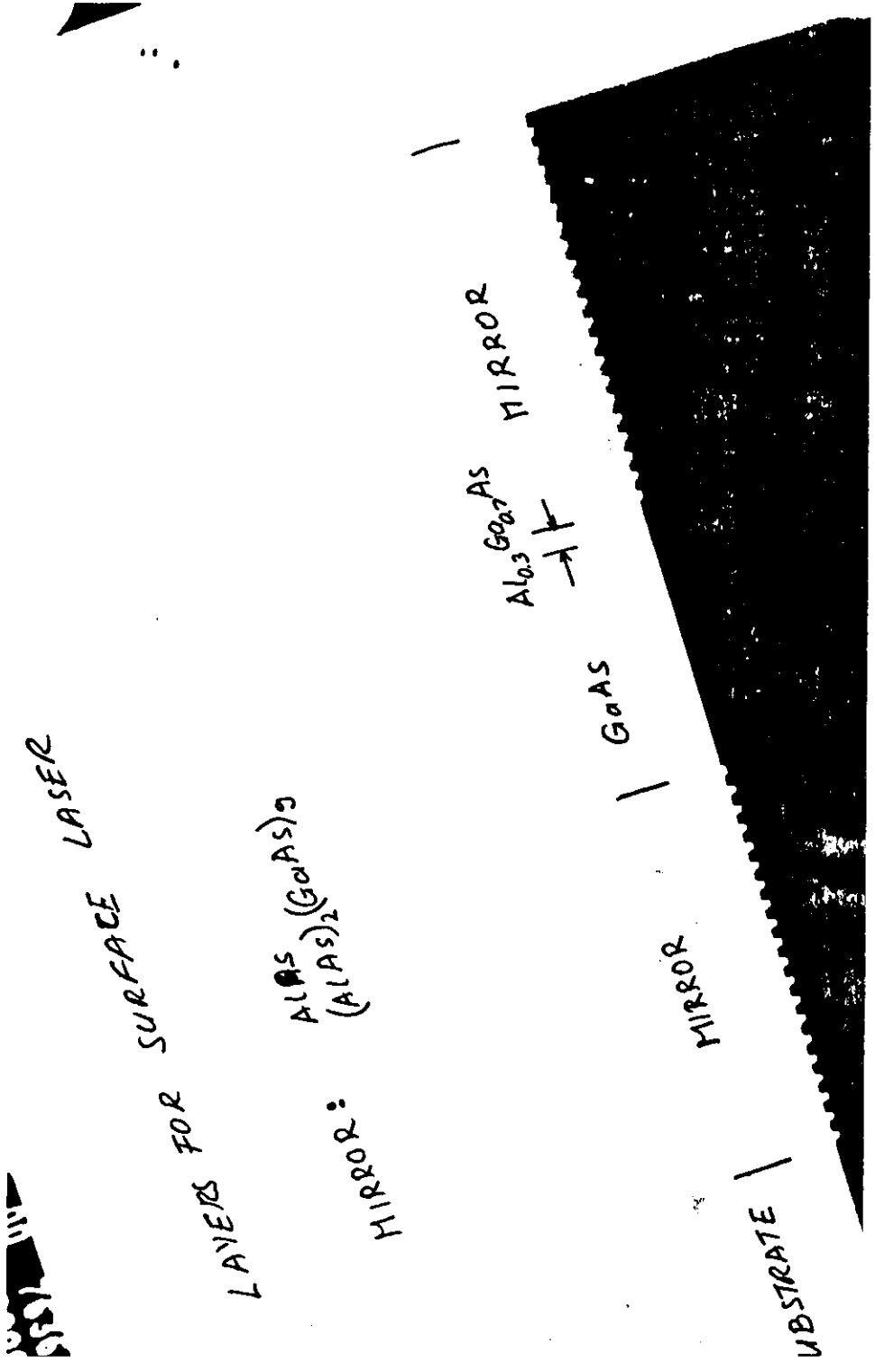

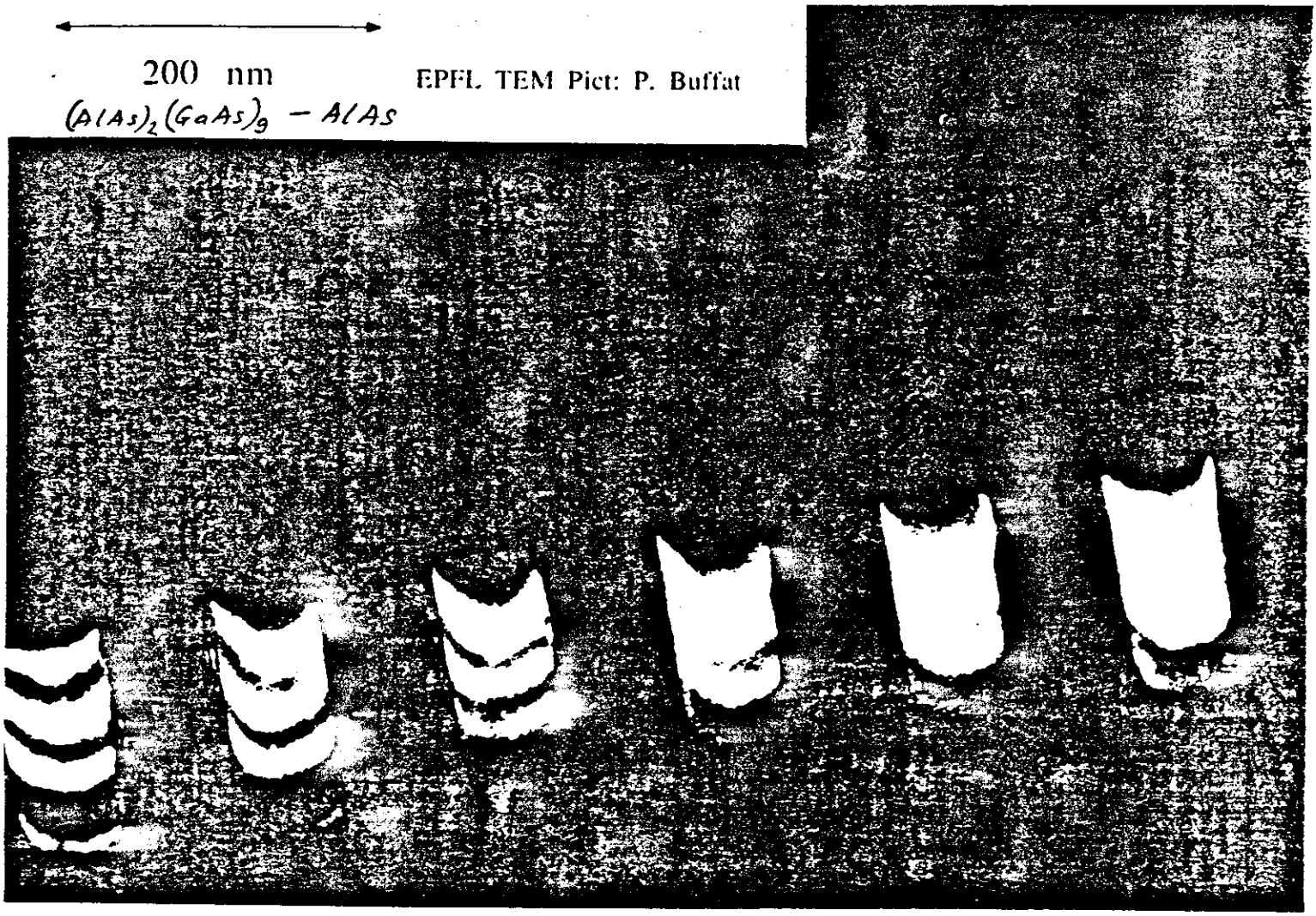
200 nm
EPFL TEM Pict: P. Buffat
$(AlAs)_2(GaAs)_9 - AlAs$

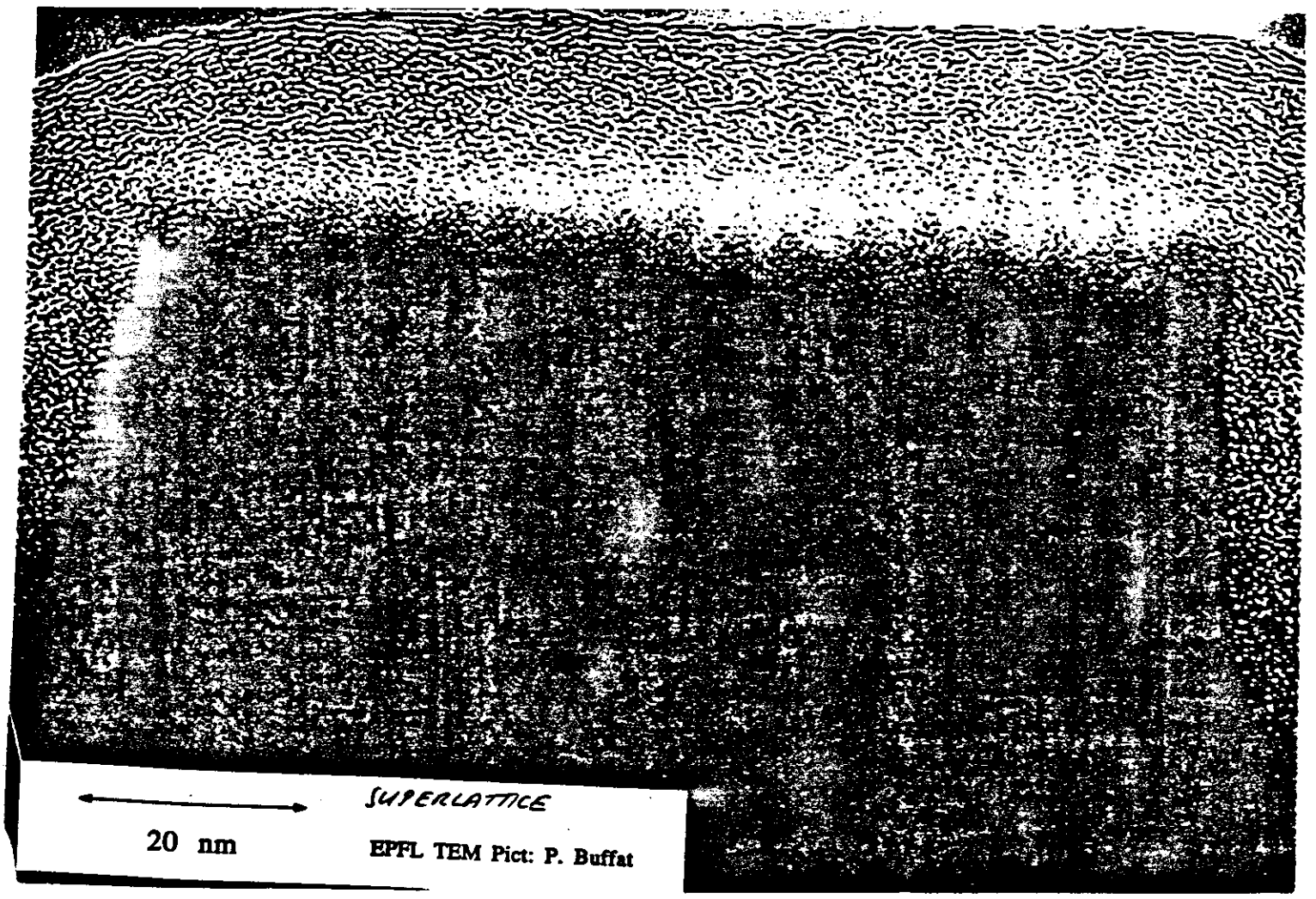
SUPERLATTICE
20 nm
EPFL TEM Pict: P. Buffat

POTENTIAL WELL STRUCTURE

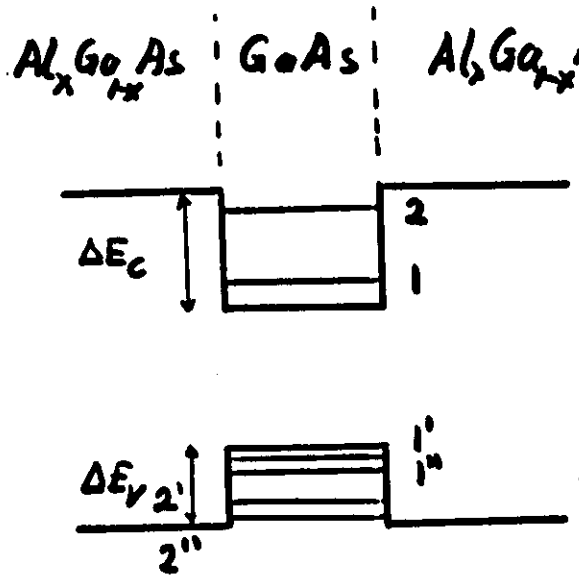

B.GAP : $Al_x Ga_{1-x} As$: E_{g1}

$GaAs$: E_{g2}

$$\Delta E = \Delta E_c + \Delta E_v = E_{g1} - E_{g2}$$

$$\Delta E = 1.25 \cdot x$$

$x = 0.4$: $\Delta E \simeq 0.5\,eV$

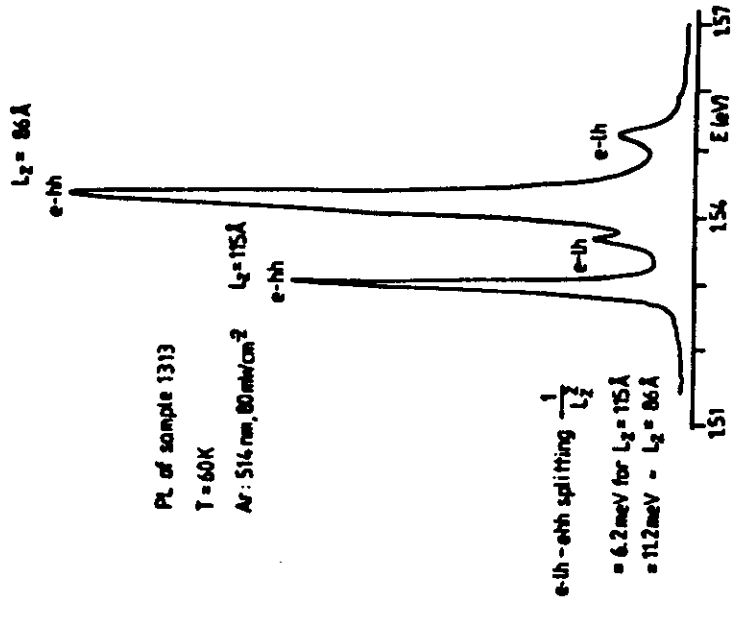

PL spectrum of MQW structure consisting of 14 QWs of 115 Å width and 86 Å wide SQW on top. Al content of barriers = 0.35

G. WEIMANN ET AL.

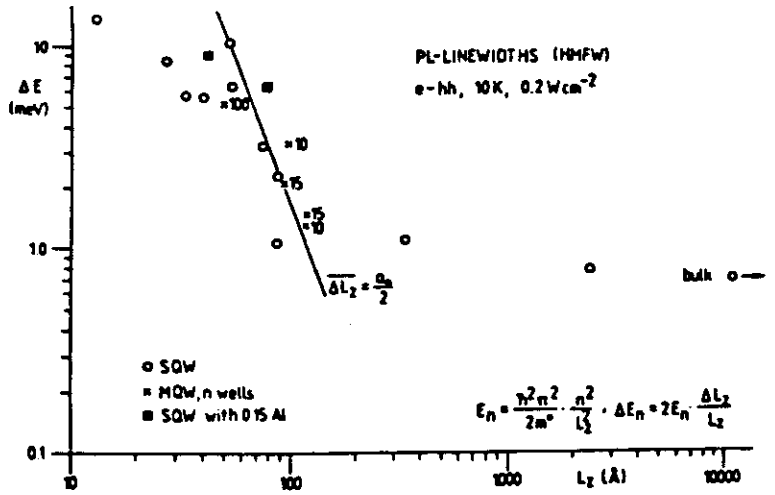

FIGURE 3
Low temperature (10 K) linewidths of e-hh emission as function of well width.

G. WEIMANN ET AL

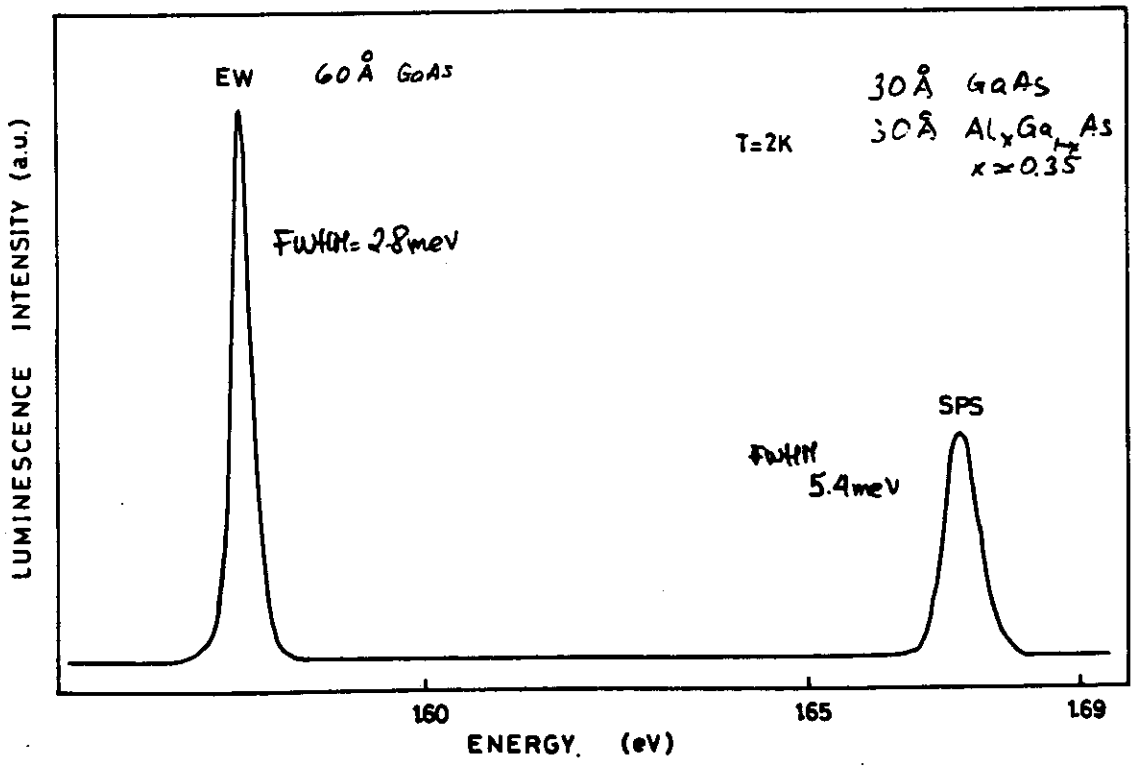

8W/cm², Ar 488μm

PHOTOLUMINESCENCE OF QW AND SUPERLATTICE

2-DIM. ELECTRON GAS STRUCTURE

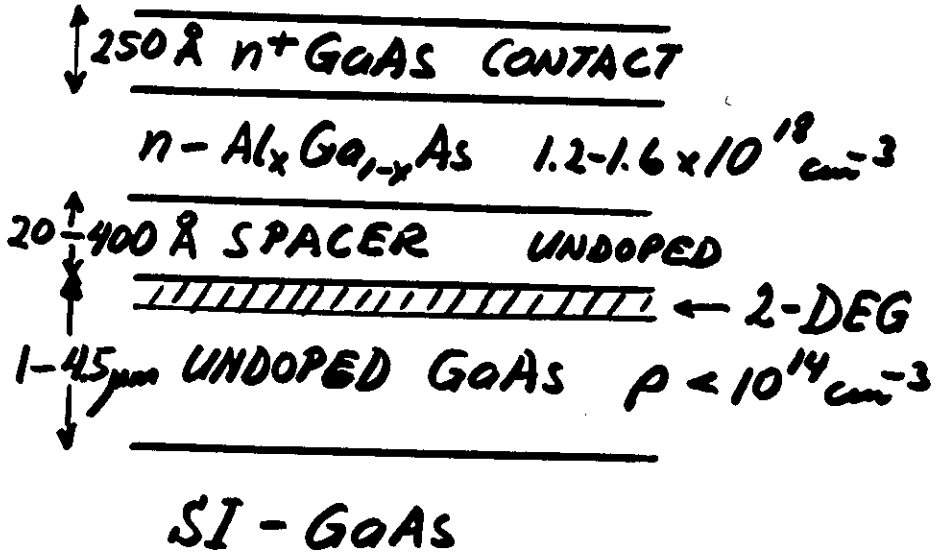

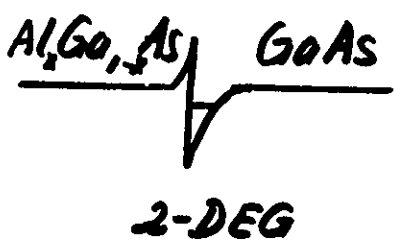

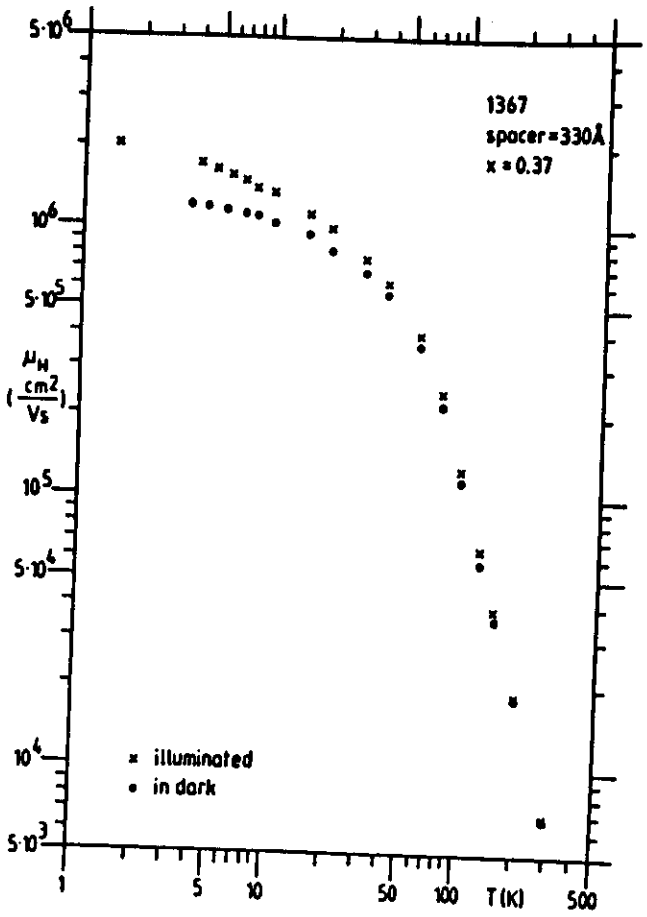

MOBILITY AS FUNCTION OF TEMPERATURE FOR 2-DEG.

G. WEIMANN ET A.

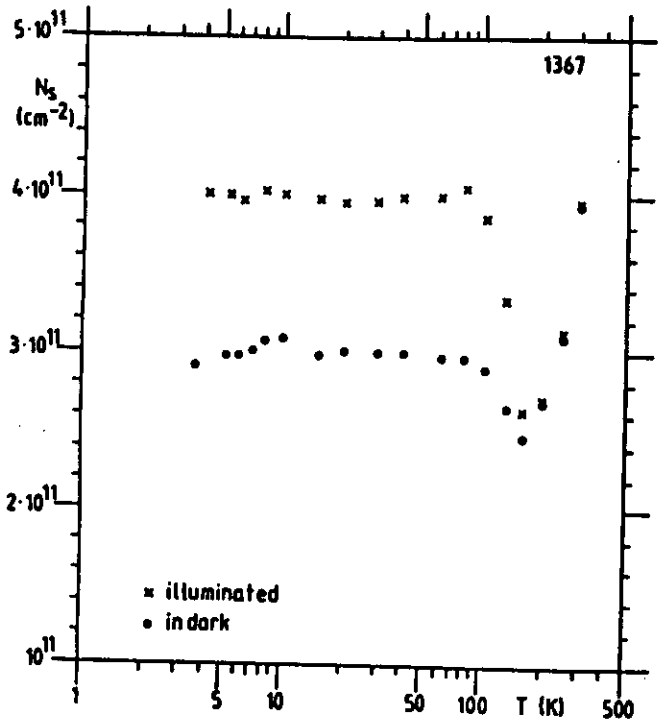

INTERFACE DENSITY OF 2DEG AS FUNCTION OF TEMPERATURE

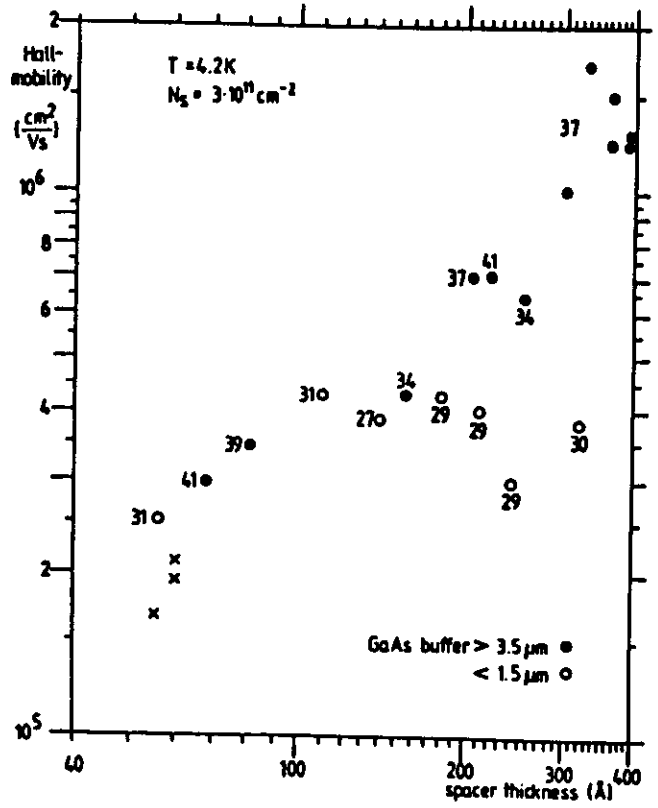

ELECTRON MOBILITY AS FUNCTION OF SPACER LAYER.

G. WEIMANN ET AL

G. WEIMANN ET AL.

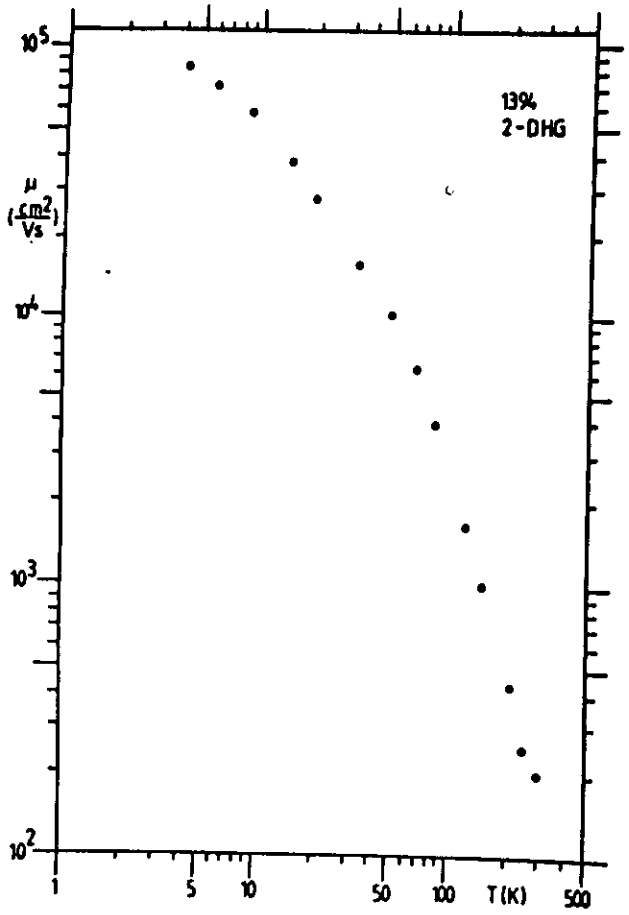

MOBILITY OF 2-D HOLE GAS (2-DHG) AS FUNCTION OF TEMPERATURE

G. UEIMANN ET AL.

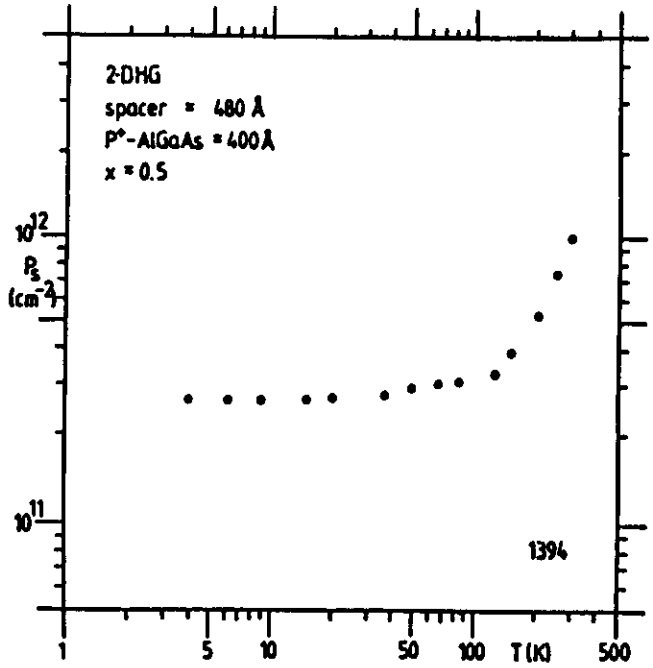

HOLE DENSITY AS FUNCTION OF TEMPERATURE

G. UEIMANN ET

III. GRATING

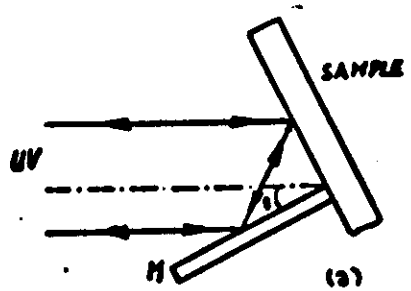

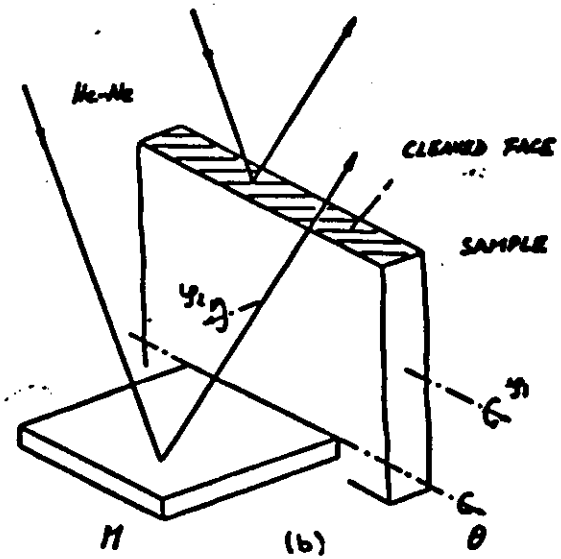

SET UP FOR GRATING FABRICATION

FABRICATION

- HOLOGRAPHY
- E-BEAM WRITING

1) EXPOSURE

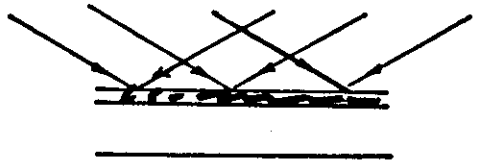

UV

PHOTO RESIST

WAVEGUIDE

SUBSTRATE

2) DEVELOP

PHOTO RESIST

WAVEGUIDE

SUBSTRATE

3) ETCH

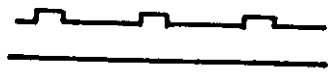

WAVEGUIDE

SUBSTRATE

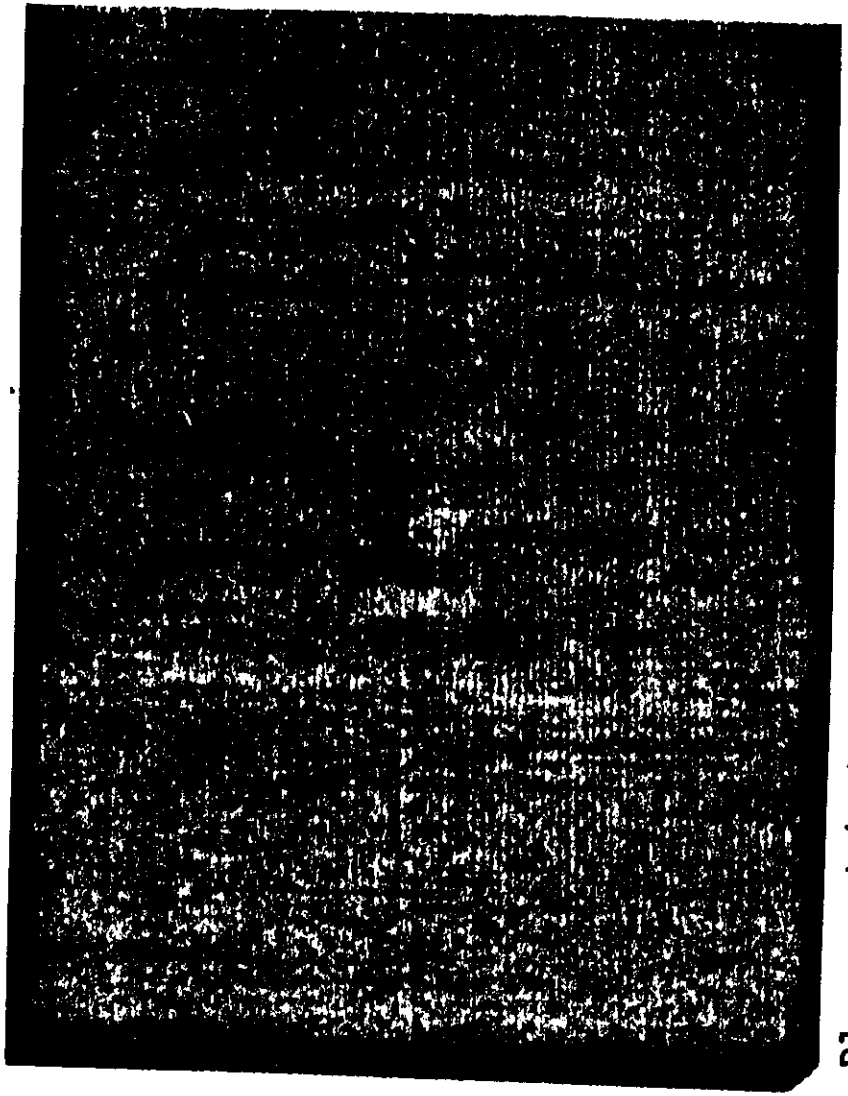

Plasma etched grating. Periodicity 0.8um

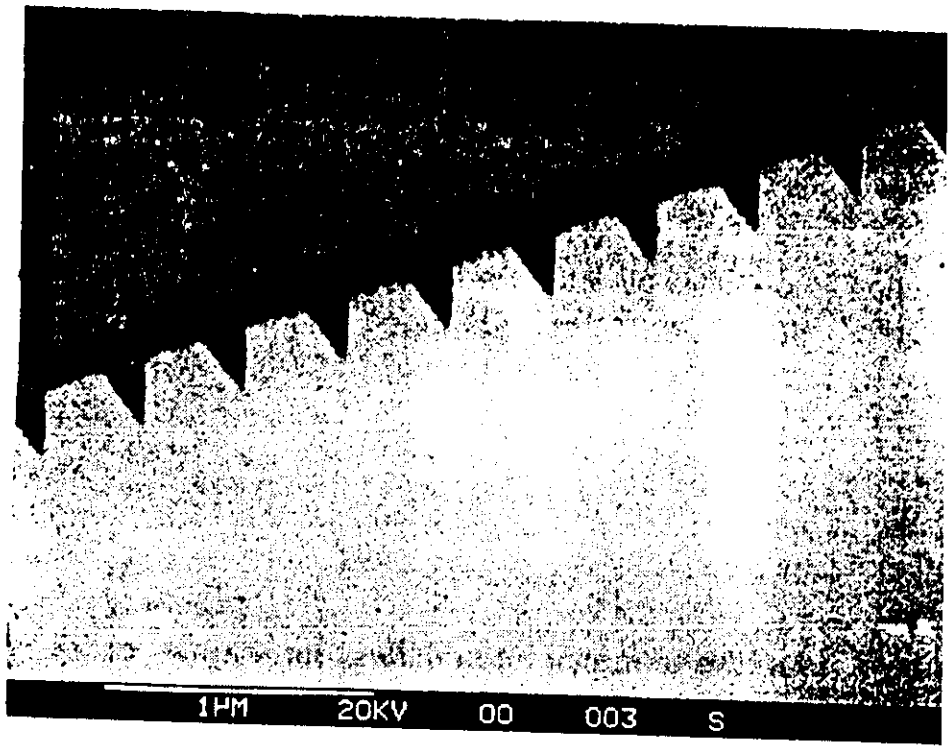

RIE GRATING

$\Lambda = 138\,nm$

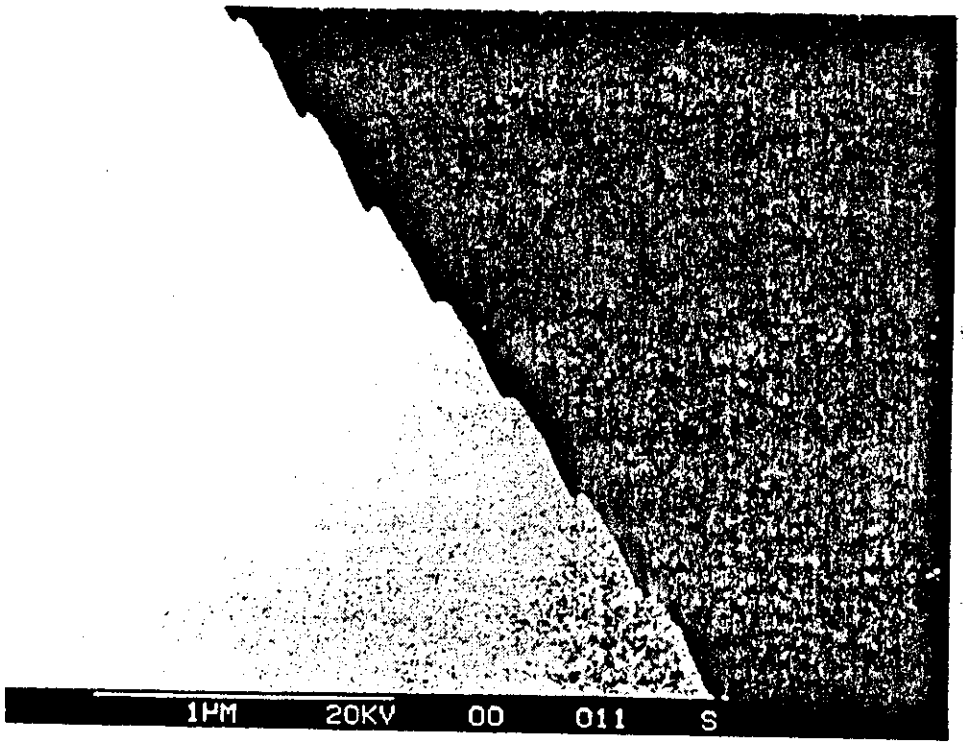

ARGON-ION BEAM MILLED GRATING

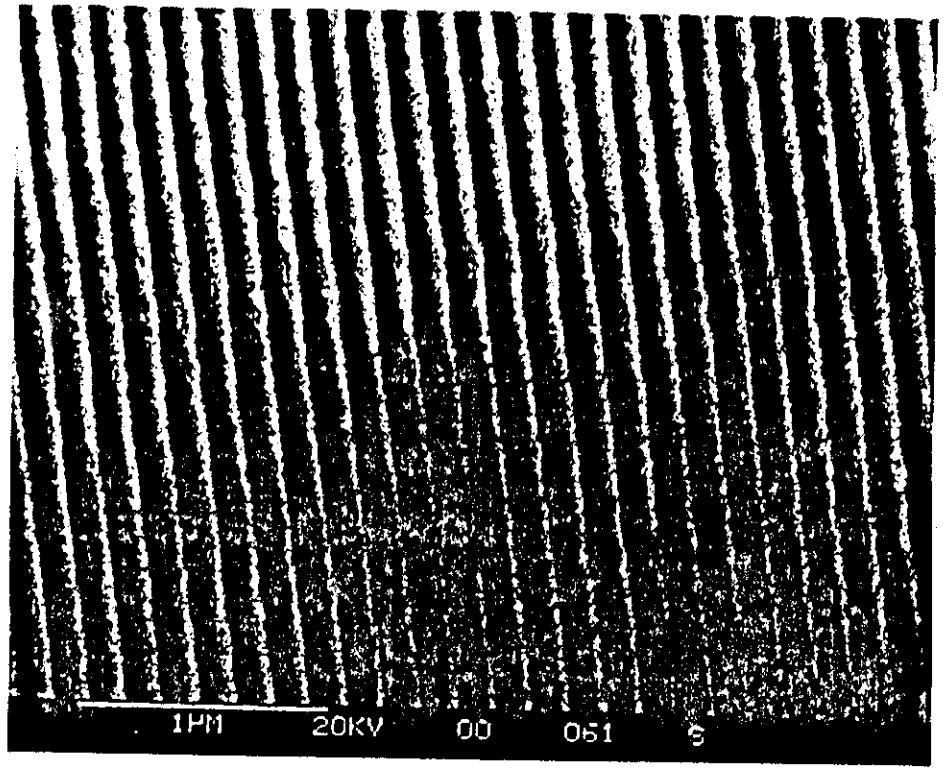

RIE-GRATING, FEATURE SIZE ~70 nm

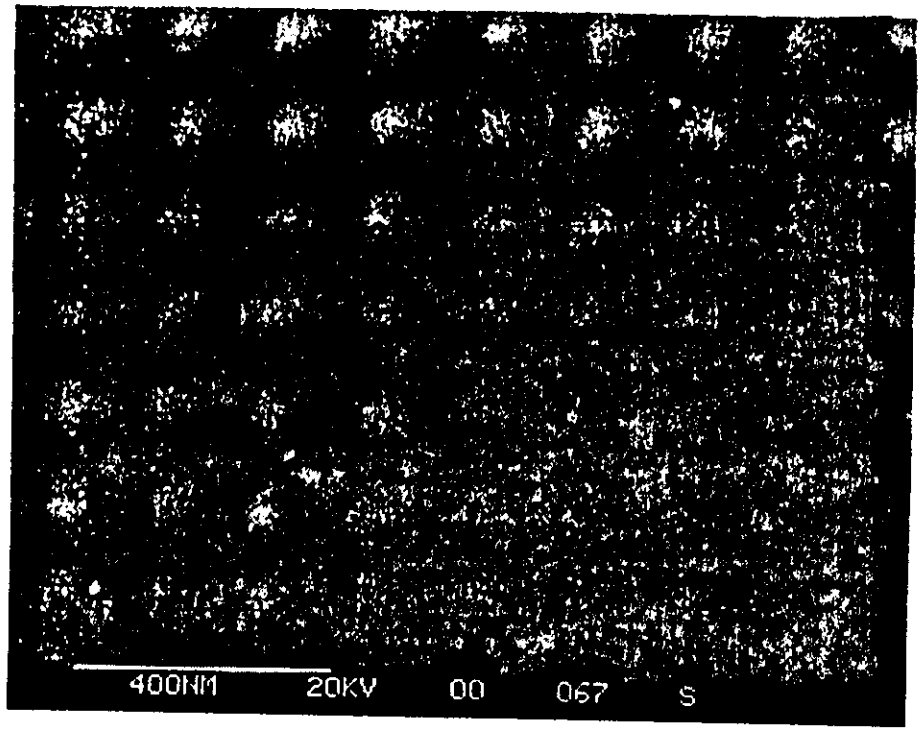

QUANTUM BOX BY HOLOGRAPHIC AND RIE PROCESSING

PRINCIPLE OF GRATING COUPLER

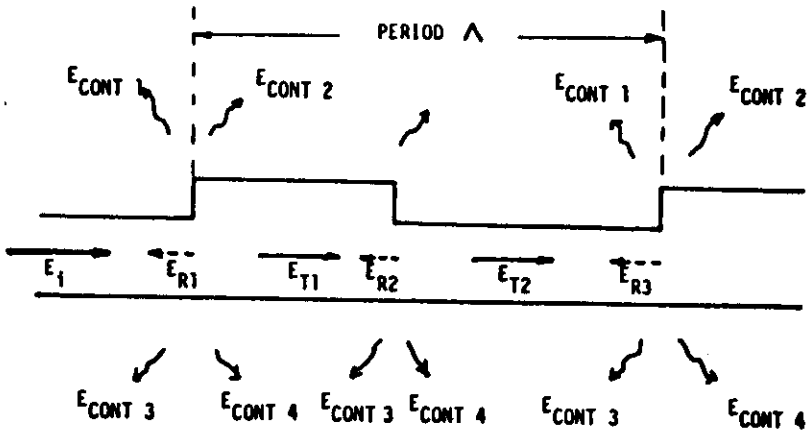

1. FOR CERTAIN ANGLES

   $E_{CONT(i)}$ ADD IN PHASE BEAM

2. FOR CERTAIN PHASES OF THE REFLECTED FIELD E_R, $E_{R(i)}$ CAN ADD TO GIVE A BACKWARD WAVE (REVERSE PROPAGATION DIRECTION TO INCIDENT WAVE).

3. SPECIAL CASES FOR DBR

a)

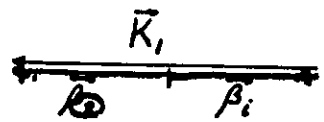

$$K_1 = \frac{2\pi}{\Lambda}$$

$$\beta_i = \beta_2 = \beta_{K_1}/2 = \pi/\Lambda_1$$

$$\Lambda_1 = \lambda/2n_e$$

TAKE : $\lambda = 0.9\,\mu m$

$n_e = 3.6$

$\Lambda_1 = 0.125\,\mu m$

IV: · WAVEGUIDE

b)

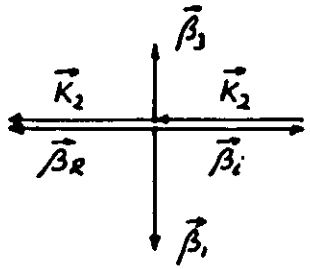

$$K_2 = \beta = 2\pi n_e/\lambda = 2\pi/\Lambda_2$$

$$\beta_1 = 2\pi n_1/\lambda \qquad \beta_3 = 2\pi n_3/\lambda$$

c)

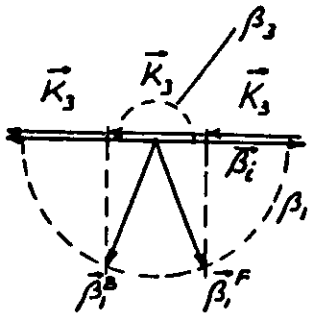

$$K_3 = 2\beta/3 = 2\pi/\Lambda_3$$

$$\Lambda_3 = 3\lambda/2n_e$$

FOR $\beta_3 < K_3/6$ NO BEAM IN MEDIUM III.

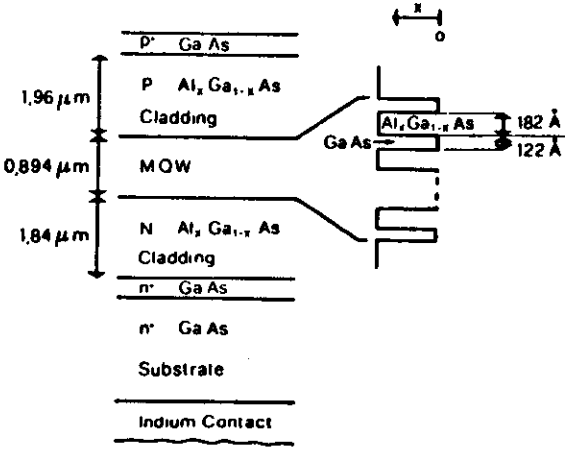

Figure 1
Schematic of the MQW structure. The insert schematically shows the Al concentration x to vary from $x = 0$ to $x = 0.24$.

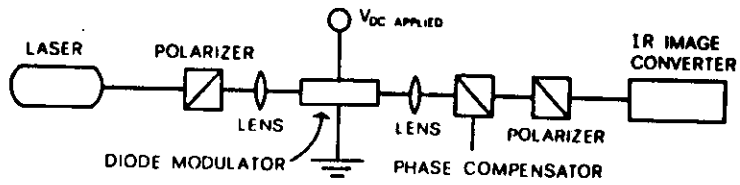

Figure 3
Experimental arrangement used for the measurement of the phase modulation.

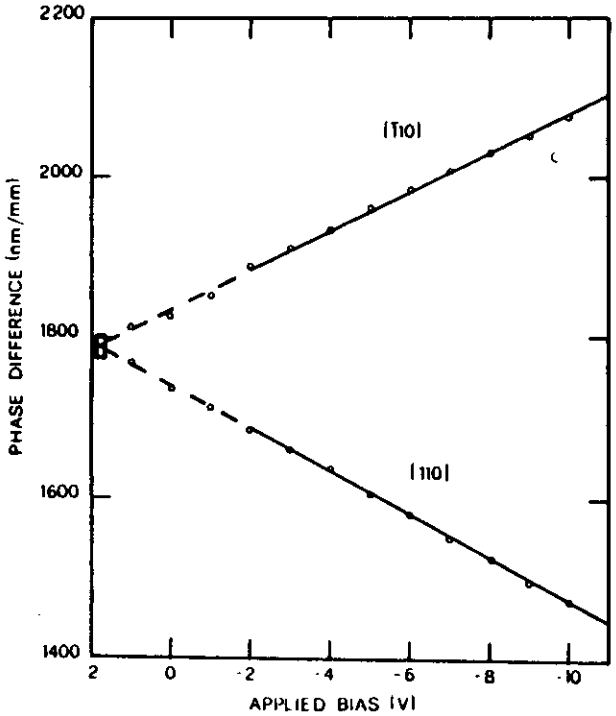

Figure 4
Phase difference between TE and TM modes as a function of the aplied bias for the two orthogonal light propagation directions along [110] and [$\bar{1}$10]. The solid lines are linear fits to the data for $V_a < -2$ V. Their extensions for $V_a > -2$ V are dashed.

p-n JUNCTION WAVEGUIDE MODULATOR

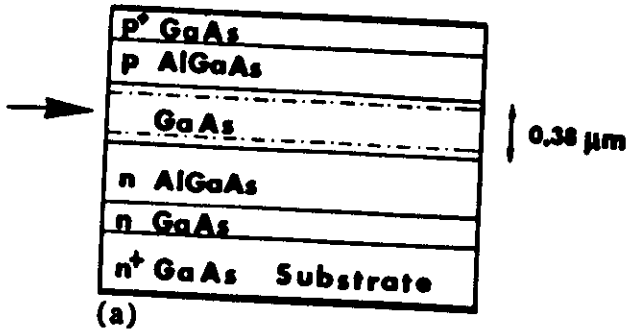

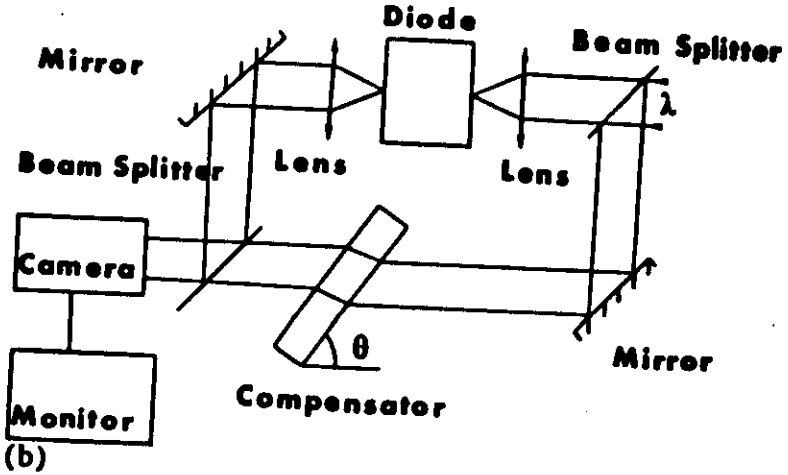

DIFFERENT WAVEGUIDE STRUCTURES

a)

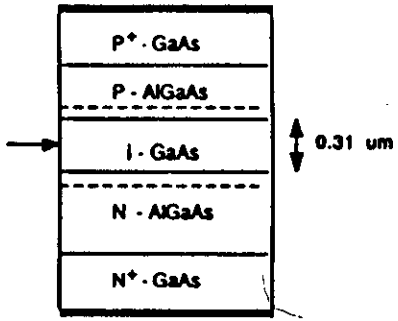

b)

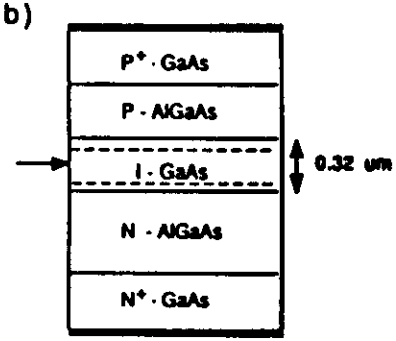

c)

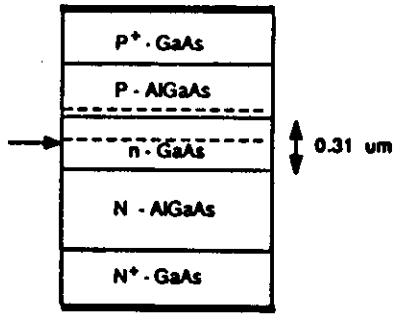

PERFORMANCE OF VARIOUS STRUCTURES

	a) Buffered intrinsic	b) Intrinsic	c) Doped active layer
0V Depletion [um]	0.32	0.16	0.055
Capacitance Cs [nf / cm2]	36	73	209
Cd [pf]	1.1	2.2	6.3
Capacitance variation [1 / V]	7%	8%	21%
♦ [rad/V-mm] λ = 1.15 um	0.45	0.87	1.33
♦ [rad/V-mm] λ = 1.09 um	0.5	1.08	1.73%
%LEO λ =1.15um	80%	43%	25%
W [pJ/rad^2-mm] λ =1.15um	5.3	2.9	3.5
W [pJ/rad-mm] λ =1.09um	4.3	1.9	2

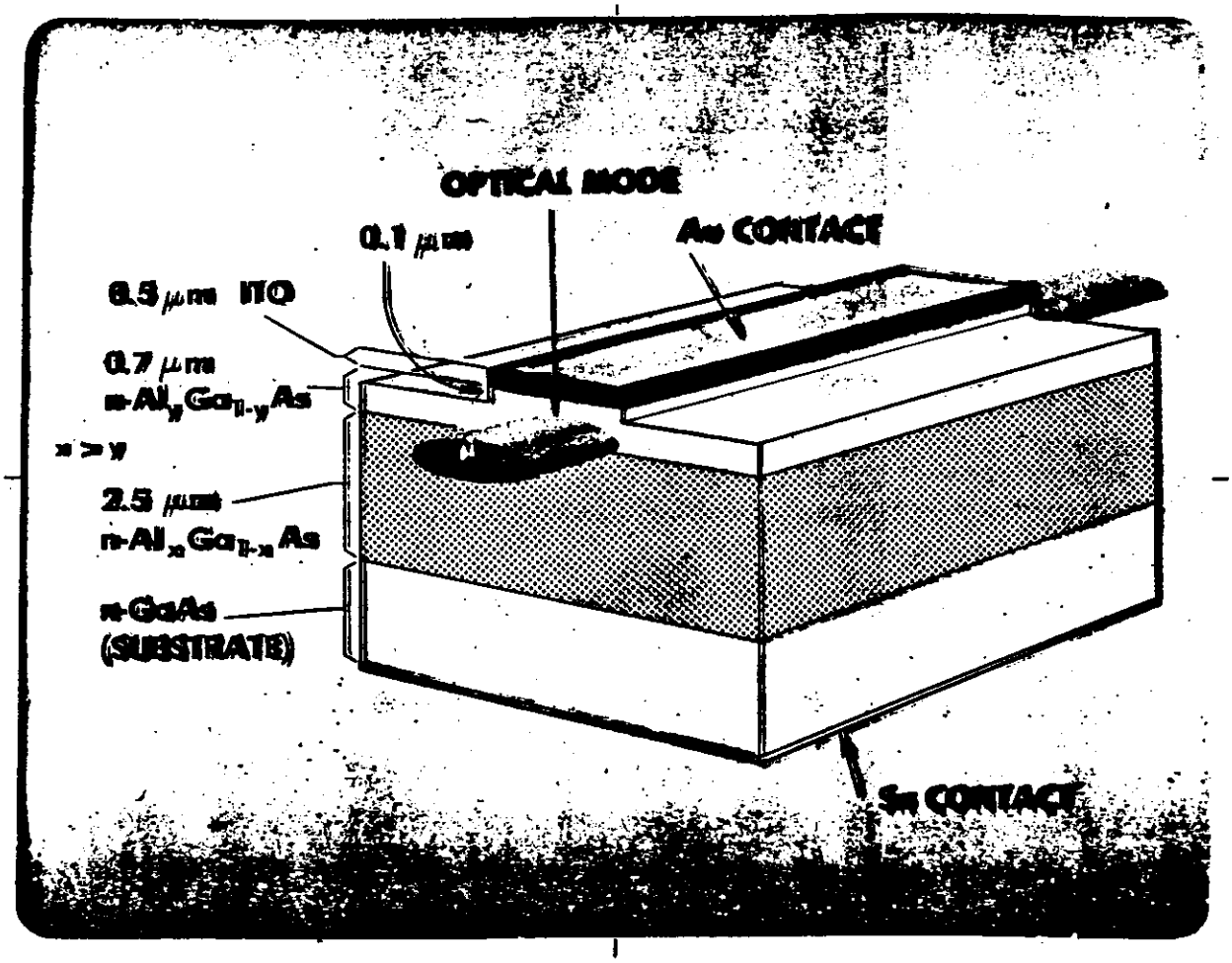

Semiconductor Waveguide Fabrication

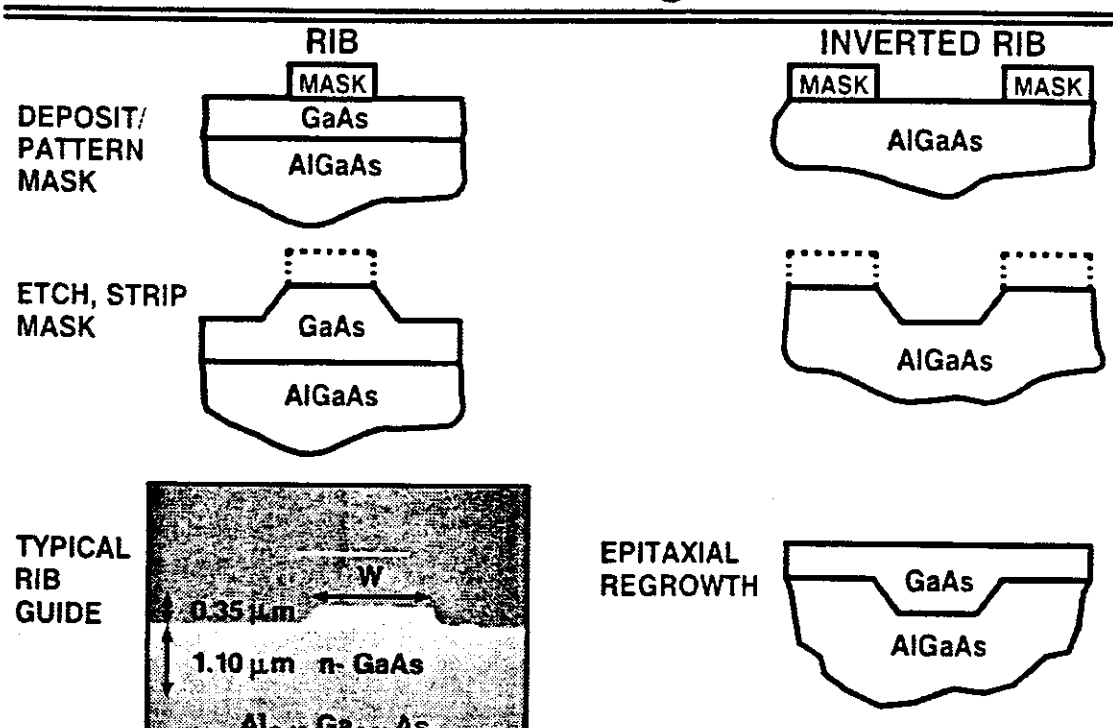

NVC87 BWT211.012

WJT
11/87

Low Loss Waveguides In GaAs

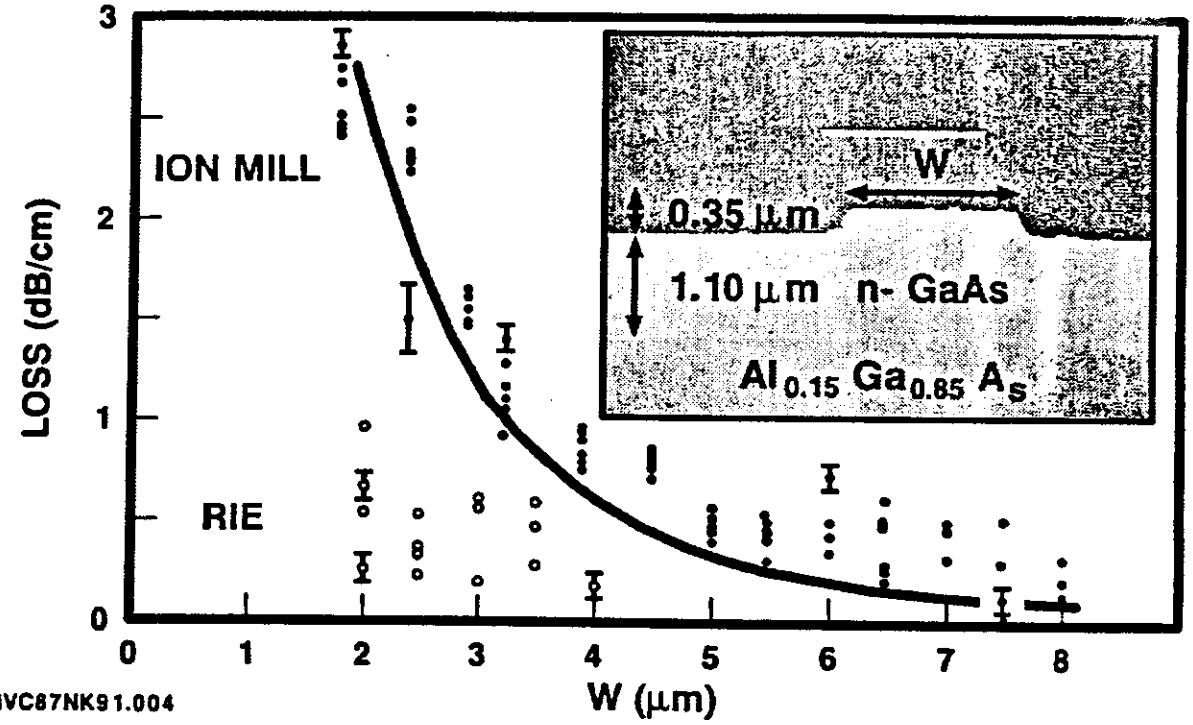

NVC87NK91.004

223

Published GaAs / AlGaAs Waveguide Loss

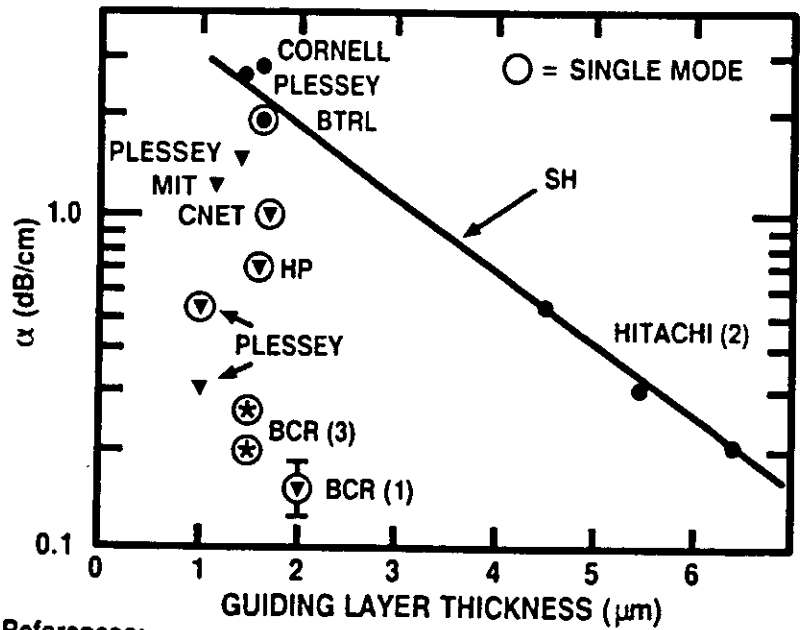

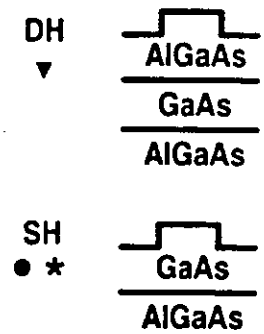

225

References:

(1) KAPON and BHAT, APL 50, 1628 (1987)

(2) HIRUMA et. al., IEEE ED-32, 2662 (1985)

(3) DERI et. al., APL 51, 789 (1987)

NVC87 BWT211.013

RJB
11/87

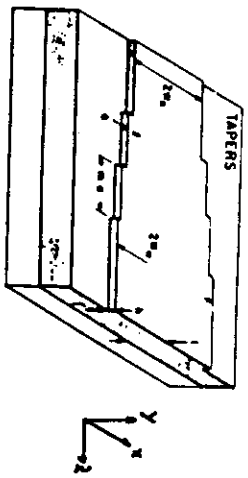

FIG. 5S Nominal shapes of waveguides. The depth z variable as y and the lateral variable as x. The overgrowing layer is shaded. It is above a cleaved $Al_xGa_{1-x}As$ Oxide, not shown in these figures, overlays the RWG, but for most of our experiments is stripped away, shown here. The lateral profile is stepped for ramps and tapers because of the raster exposure strategy of EBES. Two address units for EBES were chosen to be $a = 0.35\,\mu m$ and $a = 0.50\,\mu m$. The lateral envelopes for ramps and tapers are nominally symmetrical and linear with slope given by $1/m$.

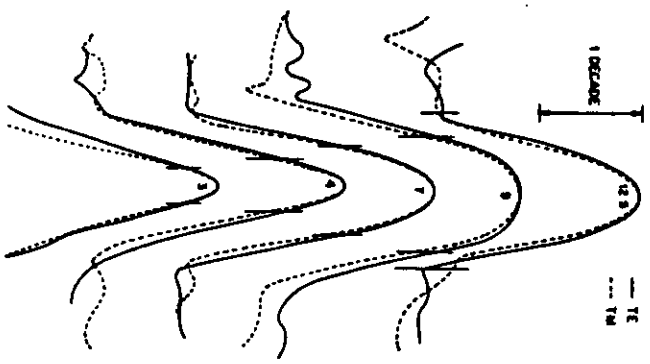

FIG. 5G Logarithmic z distributions of optical intensity for TE- and TM-like polarizations for RWG with $V = 30$ V. All output distributions are obtained by coupling from long single-mode waveguides ($2w_o = 3\,\mu m$) via lateral tapers in order to ensure reproducible excitation. The sensitive width ($w\,\mu m$) of the original rib as the reduced parameter. The fundamental mode has higher k_z and lower β, for narrower guides and for TM-like polarization.

NOTES:

SEQUENCE NO. _____

TOP

DO NOT AFFIX FLIP OVERLAYS ALONG THIS SURFACE

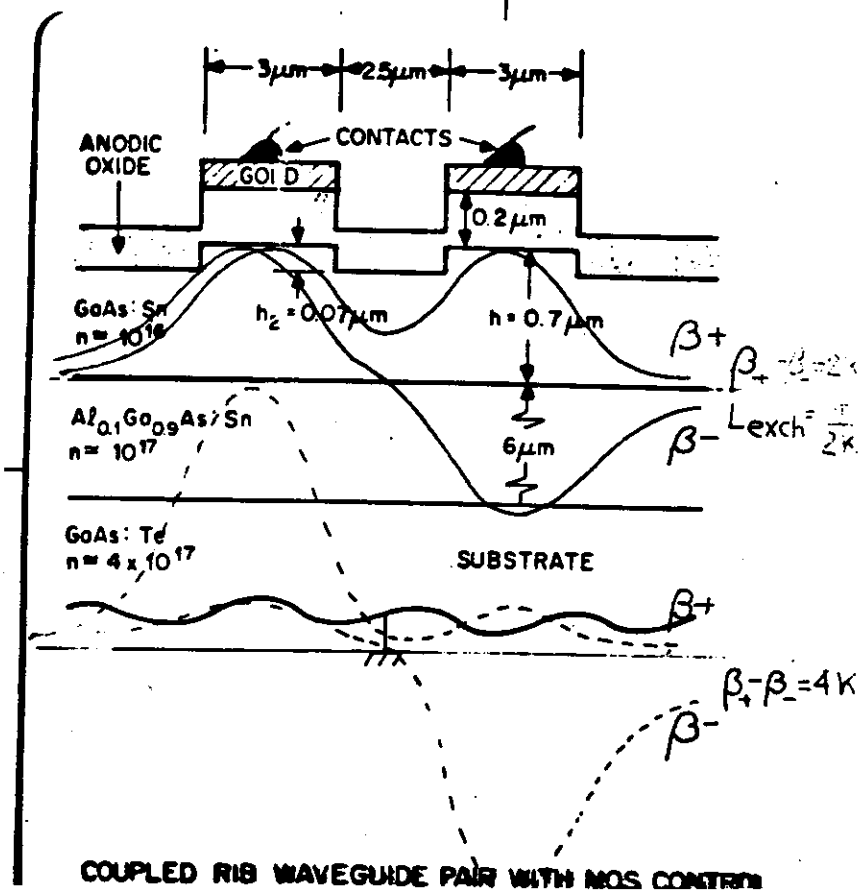

COUPLED RIB WAVEGUIDE PAIR WITH MOS CONTROL

Bell Laboratories

TOP

3 μm marks
left slave side and metal
COUPLED RIB WAVEGUIDES

GaAs RIDGE WAVEGUIDE

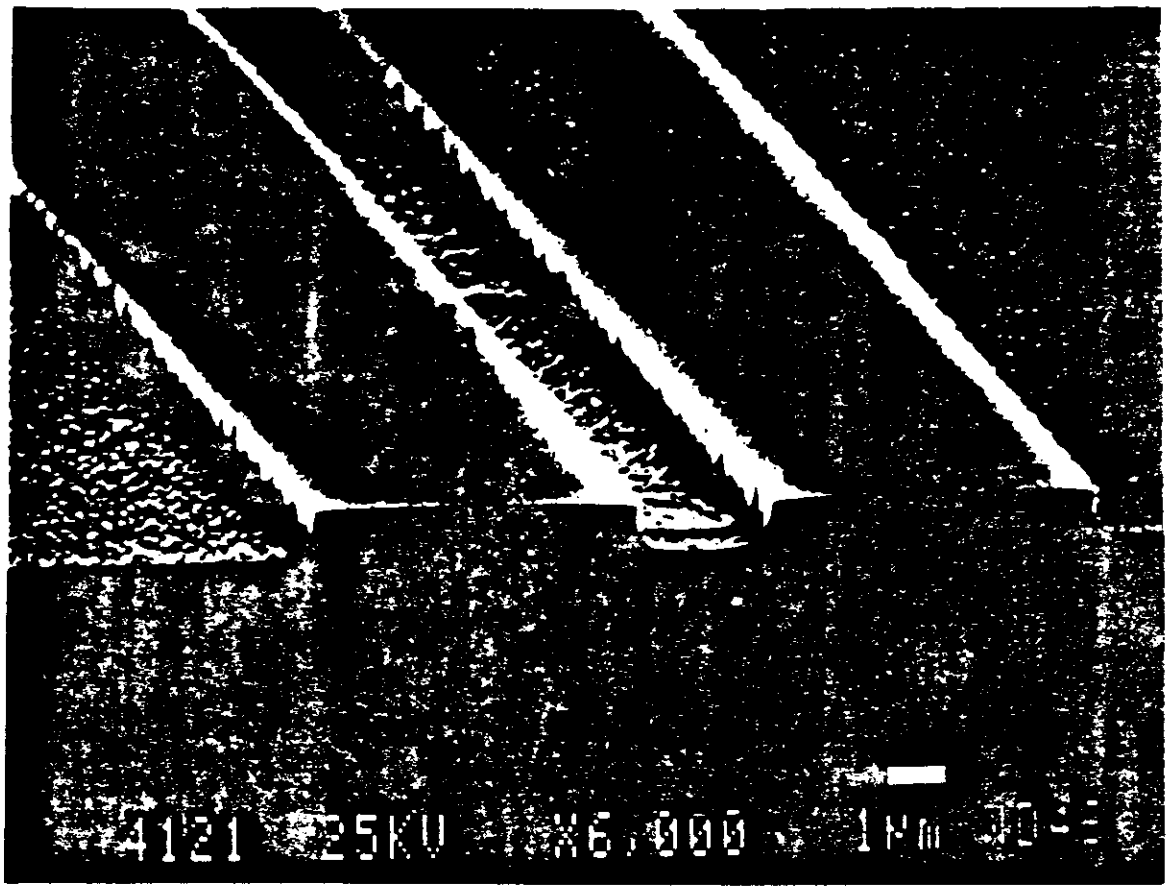

GaAs Y-JUNCTION MODULATOR

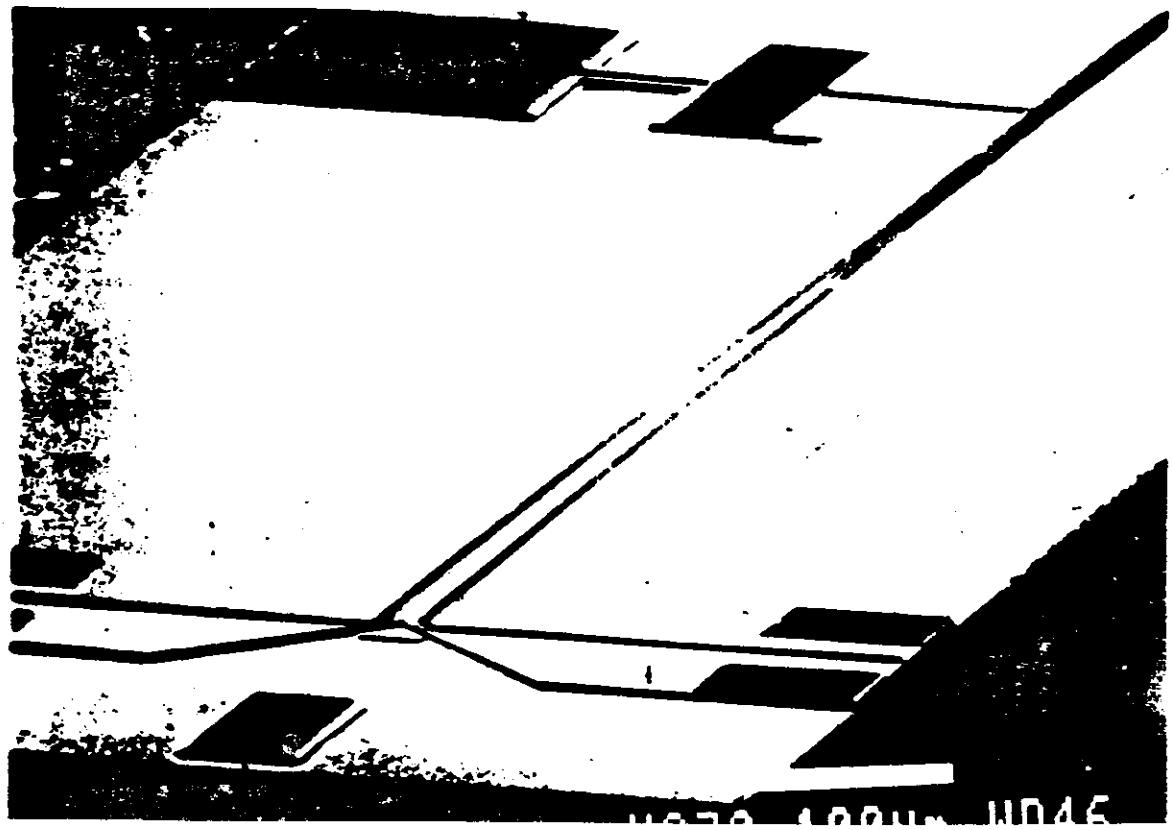

a)

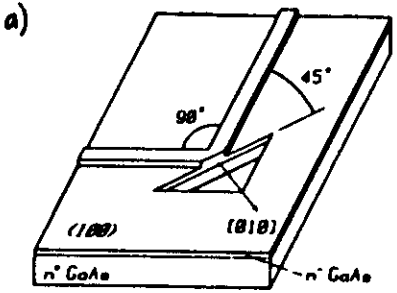

Fig.39 Schematic view of n/n+ GaAs rib waveguide mirror 10

b)

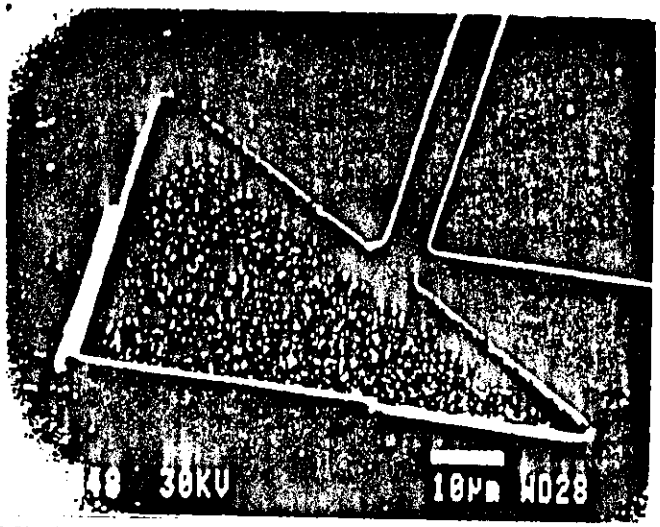

c)

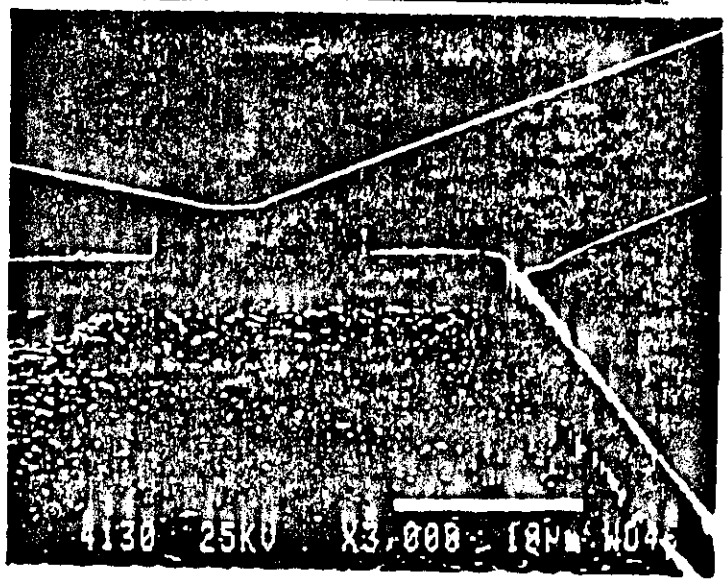

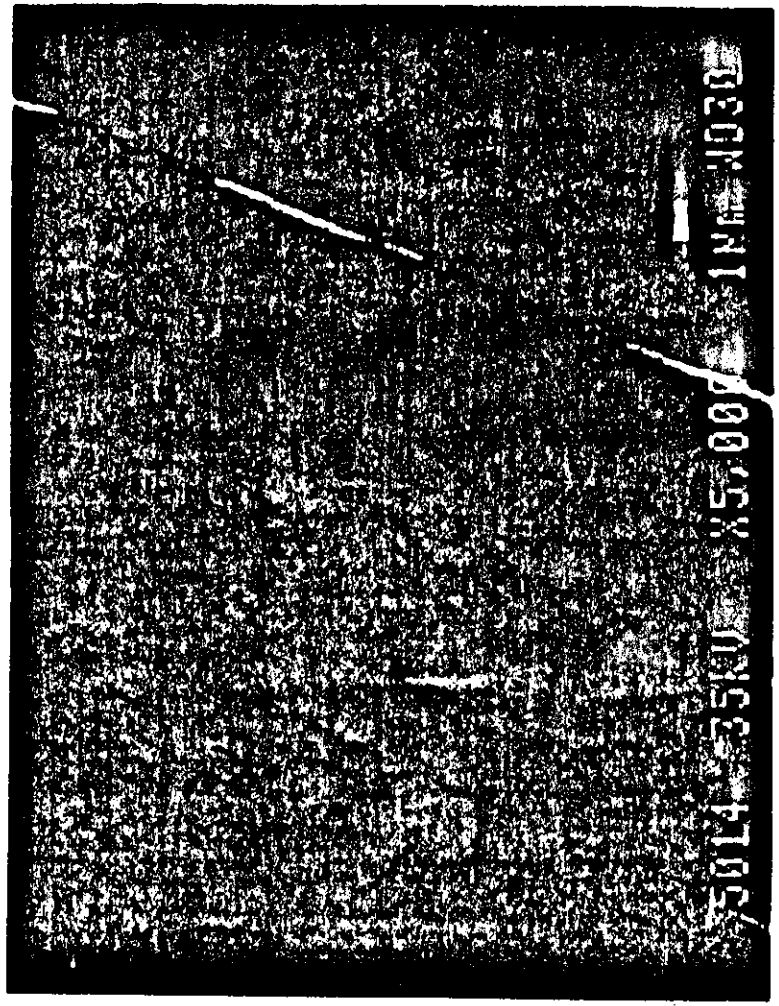

Fig.51: Y-COUPLER FOR n-n$^+$ GaAs WAVEGUIDE 14

V. FET FOR OPTICAL INTEGRATION

Siemens Forsch.- u. Entwickl.-Ber. Bd. 14 (1985) Nr. 6

InGaAs/InP:Fe Junction Field-Effect Transistor for Optoelectronic Integration

H. Albrecht, H. Huber, Ch. Lauterbach, M. Pilhal

0 Introduction

A monolithic integrated combination of photodiode and field-effect transistor (FET) in $In_{0.53}Ga_{0.47}As$/InP may in future replace the hybrid structure consisting of an InGaAs photodiode and a GaAs FET in the front end of optical receivers for wavelengths in the regions of 1.3 µm and 1.6 µm. The possibility of reducing stray capacitances in the interconnections further holds promise of improved receiver sensitivity.

Before integration is feasible, however, high-quality discrete InGaAs/InP FETs need to be developed. Since InGaAs-metal Schottky FETs cannot be fabricated with low gate current because of the low Schottky barriers [1], junction FETs (JFETs) with a diffused p–n junction are chosen [2, 3]. The present report describes the fabrication of diffused InGaAs JFETs on semi-insulating InP:Fe substrates using a self-aligned process technology and discusses their properties.

1 JFET Structure and Fabrication

Figure 1 shows a cross section through an InGaAs/InP JFET. A 1 µm thick Sn-doped $In_{0.53}Ga_{0.47}As$ layer ($N_D \approx 1.5 \cdot 10^{18}$ cm^{-3}) is grown on a semi-insulating InP:Fe substrate. The p–n junction is produced by diffusion, a sputtered Zn-doped spin-on oxide film serving as the diffusion source [3]. The resulting $p^+-In_{0.53}Ga_{0.47}As$ layer is 0.3 µm thick. Prior to the vapor deposition of the Ti/Au gate metallization, the mesa of the future JFET (250 µm by 500 µm chip) is etched using a photoresist step and a 250 µm wide stripe of semi-insulating InP:Fe substrate is laid bare for the bond pads for the drain, source and gate contacts. The further process steps are shown schematically in Figure 2. The gate structure is likewise prepared by photolitho raphy, the photoresist serving as an etching mask f the p-contact of Ti/Au as well as for patterning t $p^+-InGaAs$ layer (Figure 2b). The gate length here determined by the length of the photoresist an by the etch time. Using this process, gate lengths u to 2 µm were reproducibly realized. The T-ga formed during the etch serves as a mask for th vapor deposition of the Au–Ge/Au n-contacts fc the source and drain. This self-aligned process r sults in the sharp definition of the critical gate-t drain and gate-to-source distance without the nee for further alignment steps.

The gate contact running over the edge of th mesa initially causes a short between the p^+ lay and the n–InGaAs layer. A further photoresist ste is therefore added for selectively etching away th side of the mesa below the gate metallization dow to the semi-insulating InP:Fe substrate, in whic region the gate contact forms an air bridge. Figu 3a shows a schematic diagram of a JFET chip wit bond pads on the InP:Fe substrate for the contact The advantages gained by placing the bond pads o the InP:Fe substrate are: (i) Separation of the ga from the gate bond pad, whence (ii) the reduction stray capacitances and leakage currents, (iii) superic mechanical stability because, particularly in the ca of bonds, the p–n junction is protected from d struction. Figure 3b shows a scanning electron m crograph of the air bridge of a 3 µm gate contac

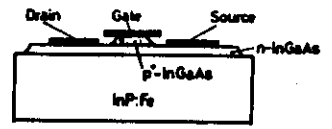

Figure 1. Cross section through an $In_{0.53}Ga_{0.47}As$/InP:Fe junc tion field-effect transistor (JFET)

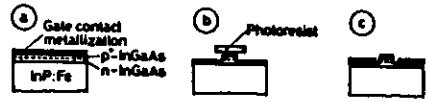

Figure 2. Process steps of the self-aligned process technology. (a Gate contact metallization, (b) Etching and fixing of gate length (c) Stripping of photoresist after source and drain metallization

Manuscript received on August 14, 1985

Dr.-Ing. Helmut Albrecht, München
Herbert Huber, München
Christl Lauterbach, München
Dipl.-Phys. Dr. rer. nat. Manfred Pilhal, München
Siemens AG, Forschungslaboratorien

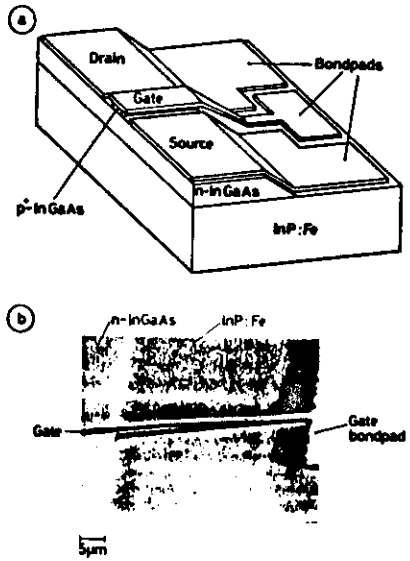

Figure 3. (a) Schematic representation of a JFET chip, (b) Scanning electron micrograph of the air bridge of a 3 µm gate contact over an InGaAs step 1.5 µm in height to the gate bond pad on the semi-insulating InP:Fe substrate

over an InGaAs step 1.5 µm in height to the gate bond on the InP:Fe substrate.

2 Properties of InGaAs/InP:Fe JFETs

Figure 4 shows the typical set of characteristics of an InGaAs/InP:Fe JFET with a gate 2 µm in length and 150 µm in width fabricated by a self-aligned process. The doping concentration of the n−InGaAs layer is $1.5 \cdot 10^{16}\,cm^{-3}$; the available channel depth is ≈0.7 µm. The maximum drain current (at the gate-source voltage $U_{GS}=0$ V) is $I_{DSS} \approx 21$ mA, where the characteristic already exhibits saturation effects at a drain-source voltage of $U_{DS} \approx 5$ V. Channel pinchoff occurs at a pinchoff voltage of $U_p \approx -6.8$ V. The difference between these two voltage values can be explained with the aid of a FET model [4] that considers the dependence of the drift velocity of the electrons in the channel on the field strength. The respective series resistances R_S between the gate and source and the gate and drain were calculated from the set of characteristics as described in [8], yielding $R_S \approx 30\,\Omega$ in each case. Figure 5 shows the transconductance g_m for a drain-source voltage of $U_D = 5$ V. The maximum transconductance g_m is 4.5 mS or, normalized to the gate width, 32 mS/mm.

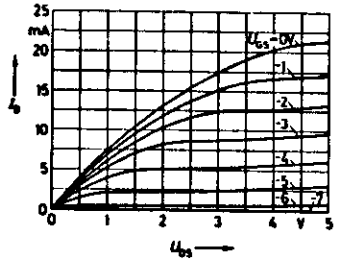

Figure 4. Set of characteristics of an $In_{0.53}Ga_{0.47}As/InP:Fe$ JFET with a gate 2 µm in length and 150 µm in width. I_D Drain current, U_{DS} Drain-source voltage, U_{GS} Gate-source voltage

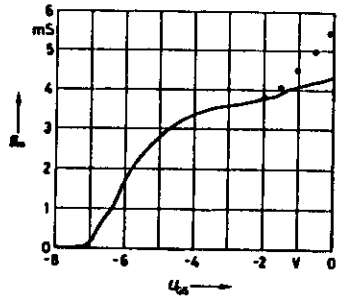

Figure 5. Transconductance g_m of the $In_{0.53}Ga_{0.47}As/InP:Fe$ JFET in Figure 4 as a function of the gate-source voltage U_{GS}. The drain-source voltage U_{DS} is 5 V. ——— Values derived from Figure 4. oooo Theoretical values for constant doping concentrations of $N_D = 1.5 \cdot 10^{16}\,cm^{-3}$

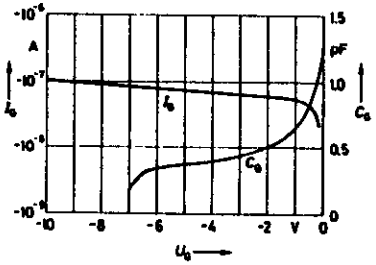

Figure 6. Gate current I_G and gate capacitance C_G as a function of the gate voltage U_G. Drain and source are at the same potential

Further key parameters relating to the use of these InGaAs/InP:Fe JFETs in monolithic integrated photodiode preamplifier combinations, which determine the noise level and consequently the receiver sensitivity, are the gate current I_G and gate capacitance C_G as a function of the gate voltage U_G. With both drain and source at the same potential (Figure 6) for $U_G = -5$ V, e.g., $I_G \approx 60$ nA and $C_G \approx 0.3$ pF were measured. The $I_G(U_G)$ characteristic was measured statistically and the $C_G(U_G)$ characteristic dynamically at a frequency of 1 MHz. The evaluation of the capacitance measurement for determining $C_G(U_G)$ is described in [5].

The gate current I_G lies between 20 nA and 100 nA, corresponding to current densities of 6.6 kA/cm² to 33 kA/cm². Due to the nonpassivated surface in the gate region, I_G is certain to include a large proportion of the surface leakage current.

3 Discussion

When the gate-source voltage U_{GS} is reduced to a value close to zero, the drain saturation current I_{Dsat} increases far less than in the case of high negative U_{GS} values (Figure 4). This is reflected in the shape of the transconductance characteristic (g_m in Figure 5) above $U_{GS} = -4$ V. This behavior is induced by the series resistance R_S in the gate-source region and the decrease in conductivity in the channel in the vicinity of the metallurgical p−n junction.

First the influence of the decrease in conductivity will be considered. Figure 7 shows the measured doping profile and drift mobility profile μ_{Dr} over the channel depth x of an InGaAs/InP:Fe JFET with a gate 100 µm in length and 200 µm in width [3]. This FATFET test structure came from the same epitaxy wafer as the short-channel FETs discussed above. The drift mobility μ_{Dr} lies in the region of 7000 cm²/Vs and is almost constant over the entire channel depth. In contrast to this, the doping profile exhibits a marked dip as the p−n junction is approached (small x) that has its origin in the indiffusion of zinc (density $N_A(x)$) into the n−InGaAs layer. This leads to a reduction in the net doping concentration $N = N_D - N_A(x)$, resulting in a parallel reduction of the free electron density

$$n(x) = N_D - N_A(x), \tag{1}$$

where N_D denotes the spatially independent donor density in the n−InGaAs. The average conductivity

$$\bar{\sigma}(x) = e\bar{\mu}_{Dr}\bar{n} = \frac{e\mu_n}{a-x}\int_x^a n(x')\,dx' \tag{2}$$

increases correspondingly slowly as small values of x are approached, this being ultimately reflected in the slight increase in I_{Dsat} at low values of U_{GS}. In (2), e denotes the elementary charge and a the available channel depth. To realize optimal values for the saturation current I_{Dsat} and the transconductance g_m a constant n-doping up to the edge of the p−n junction would therefore be advantageous. The theoretical transconductance characteristic in the region of low U_{GS} values in the case of a constant doping concentration of $n = 1.5 \cdot 10^{16}\,cm^{-3}$, corresponding to the maximum doping concentration in Figure 7, is indicated in Figure 5.

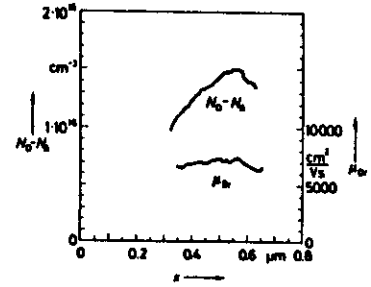

Figure 7. Doping profile $N_D - N_A$ and drift mobility profile μ_{Dr} as a function of the channel width x of an $In_{0.53}Ga_{0.47}As/InP:Fe$ JFET with a gate 100 µm in length and 200 µm in width

The series resistance R_S enhances these effects but has little influence on the JFETs of relatively low transconductance considered here. With the saturation current I_{Dsat} only the voltage $U_{GS} - R_S I_{Dsat}$ is effective on account of the voltage drop $R_S I_{Dsat}$. The transconductance $\tilde{g}_m$ (Figure 5) calculated from the measured characteristics is related to the internal transconductance g_i ($R_S = 0$) of the JFET corresponding to [7]

$$g_m = \frac{g_i}{1 + g_i R_S}. \tag{3}$$

For $g_m = 4.5$ mS (Figure 5, $U_{GS} = 0$) and $R_S = 30\,\Omega$, the internal transconductance g_i calculates with (3) at 5 mS. Considerably larger improvements are to be expected, however, from JFETs with higher g_m values and the same R_S. In some of the JFETs with a gate length of 2 µm the drain current was observed to increase in the saturation region with increasing U_{DS} in the case of high U_{DS} values. This effect, which reduces the drain-source resistance, is induced by an additional rise in current due to a concentration of impurity centers in the region of the InGaAs/InP:Fe interface. This can be avoided by interposing an undoped buffer layer between the InGaAs and the InP:Fe substrate or by the realization of better InP:Fe substrate properties.

4 Outlook

Self-aligned InGaAs/InP:Fe JFETs with bond pads for the source, drain and gate contacts brought out on the InP:Fe substrate were implemented. Bonded JFET chips with a gate length of 2 µm and a channel doping concentration of $1.5 \cdot 10^{16}\,cm^{-3}$ show gate currents lower than 100 nA with a good current saturation behavior. The slight increase in

VI. MONOLITHIC APPROACHES

1. INTEGRATION LEVELS

The difficulty to interconnect devices increases with the number of components and/or interfaces. To reduce the number of interfaces, future integration trends are, therefore, directed towards a monolithic approach, where a majority of devices are directly fabricated on a common substrate. Inspection of Table I reveals that almost all the devices listed can be made with III-V semiconductor materials. Direct energy gap materials that can be epitaxially grown by lattice matching to a suitable chosen substrate (e.g. $Al_xGa_{1-x}As$-GaAs, $In_{1-y}Ga_xAs_{1-y}P_y$-InP etc.) are preferred. It should be noted here that Si is a poor electrooptical material because it possesses an indirect fundamental band gap and a center of symmetry which forbides a linear electrooptic (Pockels) effect suitable for phase modulation. But Si possesses good mechanical and electrical properties that may make its use a substrate and electrically active material very attractive.

As any optical system requires the signals to be converted electro-optically, one can identify three types of monolithic integration efforts : a) electrical-optical component integration, b) optical-optical component integration and c) combination of a) and b). These types of integration efforts experience also various levels of complexity. Intuitively, it might be tied to the number of device components on a given substrate. As batch processing permits the fabrication of many devices simultaneously, this is not necessarily so : the fabrication of a laser array is actually slightly simpler than that of an individual laser, as long as the array components need not to be addressed individually. The level of complexity is thus preferably

judged by the difficulty of the fabrication and/or assembly steps and the sophistication of the eventual system requirements. The mutual compatibility of all physical parameters, fabrication steps and system aspects are a prerequisite to any integration effort. In the following, some of the considerations will be discussed along with a) and b). As research and development efforts are preoccupied with a) and b), we will forego discussion of c).

2. ELECTRICAL-OPTICAL INTEGRATION

The integration of a detector with a preamplifier is compatible with conventional electronic integration. The only optical requirement is to achieve the highest conversion efficiency possible. The primary advantage of this integration step lies in the elimination of parasitic impedances that will improve the speed and sensitivity of the detectors.

The integration of a laser with an electrical driver already poses a severe restriction because a laser needs an optical feedback mechanism besides the optical gain. Early integration attempts relied on cleaved laser mirrors that strongly limited the substrate length. This reduces the possibilities to arrange and design the transistors. Removal of the heat may also become a problem because the lasers are high current density devices ($j \simeq 10^3$ A/cm^2) and sensitive to temperature. In addition, the semiconductor layer properties of the transistor differ with those of the laser. The growth cycle for the layer fabrication for this type of integration has to be modified. The active layer of the laser is embedded in highly conductive, but low index cladding layers to isolate the optical modes from the contacts and the substrate

material. Accordingly, the fabrication of an integrated laser and driver can no longer be on the same physical plane.

This brief discussion only serves to underline the great challenge posed by the electrical-optical integration. M. Hirao et al.[1] recently presented a complex driver circuit integrated with a laser. The high quality of the driver was obtained by fabricating one laser mirror by reactive ion etching. The latter process only resulted in a small degradation of the laser output efficiency. This success demonstrates a first step of a fully integrated optical repeater based on a detector-electrical amplifier-regenerator-driver-laser combination. Dr.Casey will discuss the progress in this domaine in a companion Seminar.

3. OPTICAL-OPTICAL INTEGRATION

3.1. APPROACHES

The integration of optical modulators with other optical waveguide components such as bends, branch couplers and/or tapers to form individual switches and switching arrays can be controlled with planar technology. Similarly the formation of laser arrays only becomes complicated if the interconnecting electrodes are separated (see Fig. 1.). Optical waveguide devices that contain semiconductor lasers must also provide means for heat sinks, electrical contacts, feedback and possible monitoring circuits. The integration of a laser with a detector requires at least a particular solution of the feedback problem. As this combination opens up new possibilities, a brief discussion of recent developments appears appropriate. Figure 2 shows a schematical arrangement of a semiconductor laser with an optical detector to monitor the laser emission. In this arrangement the laser section is formed between the mirrors M_1 and M_2. The

detector lies between mirrors M_3 and M_4. Preferably all the mirrors are formed by reactive ion etching in plasma (RIE) with the possible exception of M_1 and M_4. The gap between M_2 and M_3 should not exceed 5 µm for efficient coupling of the laser radiation into the detector. The etched mirrors need to be very flat (preferably better than $\lambda/10$). Deviations from the mirror planarity result in scattering loss and poor radiation patterns but cause only a weak increase of the laser threshold current. As this integrated structure requires no special crystal growth and the mirrors are fabricated by RIE, the fabrication technology is completely planar.

The advantages of this structure are striking : Lasers can be tested before final mounting with their built in selfaligned monitor. There is no need for a complex assembly as in present commercial structures where a special monitor diode has to be aligned with the laser. New device possibilities are obtained : a) C^3-lasers[2] with (or without) integrated detectors, b) the integration of laterally phase coupled[3] laser sections of different lengths provides a frequency stabilized emission similar to that of C^3-lasers. But the operating stability of these new devices is potentially higher than those based on cleaving because of improved mechanical and thermal stability.

One of the most challenging subjects in integrated optics is the integration of semiconductor lasers with other optical waveguide components. This type of integration will enable to control complex optical interactions and permit novel optical functions. The requirements for semiconductor lasers and amplifiers (active devices), modulators and waveguides (passive devices), are summarized in

Table II . As lasers and optical amplifiers are high gain devices, they can tolerate a relatively high scattering loss if compared to passive components. But they require strong optical waveguides and optical feedback for efficient and reliable operation. In contrast to passive waveguides, lasers have also high operating current densities and operate very close to the bandgap. For this reason the active laser material would show high losses if used for optically passive devices.

Fortunately, a number of III-V compounds form complete solid solutions that can be grown epitaxially to give a wide range of possible bandgaps and optical dielectric constants. Starting with the basic epitaxial growth techniques such as liquid phase epitaxy (LPE), molecular beam epitaxy (MBE) and metal organic chemical vapour deposition (MoCVD), a variety of active and passive device integration possibilities are obtained. They are schematically represented by Fig.3.

The separation of passive and active device functions can be achieved by processing of a layer growth sequence as indicated by Fig. 3a). Energy transfer is obtained through modal interactions that couple the active layer modes with the passive ones. Feedback can be introduced by etching vertical mirrors and/or fabricating gratings (DBR) on the passive waveguide sections after the active region has been removed by etching. This approach was pioneered by Y. Suematsu and is actively persued.[4]

The second method is also based on regular epitaxial growth of cladding and active layers. Subsequent lithographic and etching steps define the active regions. The passive waveguides are obtained by a second growth cycle (often referred to as regrowth) as shown by Fig. 3b. This complex technology can in principal be applied with any epitaxial method. But it requires a very high degree of control of both etching and growth rates. Residual contaminants left over from the processing steps prior to the regrowth must be avoided. The active guide energy is transferred by butt coupling the efficiency of which is controlled by the overlaps of the active and passive model fields. Due to the similarity of the indices of refraction the reflectivity at the butt is quite low unless special separating layers are introduced.

Figure 3c represents an approach with MBE and LPE when local growth is controlled by means of masks. Suitable masks are Si and refratory materials for MBE and Al_2O_3 for LPE. The active and passive regions so defined can be made to have tapered ends as indicated in Fig. 3c. The tapering of the layers permits the adiabatic conversion of the modes associated with the active and passive region. For smooth tapered layer sections the mode coupling efficiency approaches 100 %. This structure thereby lacks useful reflection for feedback purposes in laser devices. To grow contiguous layers of different composition and/or doping is feasible with LPE, where the melts can be separated by a spacer. This results in a structure according to Fig. 4d.

The various methods give a wide range of possibilities to solve the basic interconnection problem between active and passive waveguide sections in a monolithic fashion. With the same techniques it should also be feasible to control the doping levels laterally to also facilitate electrical integration.

As already pointed out above, the crystal growth methods do not provide good control of the feedback needed for laser integration. Etching the mirror facets by RIE is not always a good solution in many cases. The application of DBR and DFB principles are very worthwhile, because of their frequency selecting and stabilizing properties. In cases where regrowth is not desirable, DBR looks very attractive as the necessary grating fabrication can be a final processing step. Feedback based on DFB is generally difficult to achieve without a regrowth step. Advanced growth and processing methods must be developed to overcome those very fundamental problems. However, for certain applications we may also use mirrors cleaved in the passive section.

Some results of modified crystal growth are represented by Figs. 4 and 5. Figure 4a shows the selectively excited luminescence of an active layer grown by the modified LPE with an Al_2O_3 mask.[5] The nominal cross section of the layers are given by Fig. 4b. The photomicrograph of Fig.5 depicts the tapered regions of an angle lapped cross section of the active layer grown by masked MBE.[6] The length of the tapered region can be reduced by decreasing the distance of the mask from the substrate. Based on such modified crystal growth, a number of applications to form integrated optical devices with novel functions are possible. Three examples will be discussed to indicate some possibilities on the integration level and its function.

3.2. TAPER COUPLED LASERS

The integration of passive waveguides by means of taper coupling as discussed above can potentially lead to an improved performance of cleaved laser devices : (i) Taper coupling provides a means of burying

the active region in a passive matrix. Current injection and non radiative recombination at the mirrors can thus be completely suppressed. The major cause for mirror degradation is thus eliminated. ii) The passive waveguides can be designed to act as strong mode filters and mode transformers. The mode filtering enhances the oscillating transverse mode stability, and the mode transformer facilitates coupling to internal and external waveguides. iii) A monomode passive filter is very effective to discriminate against spontaneous light. This will reduce the optical oscillating line width and favour of single frequency operation. iv) The incorporation of frequency filters (e.g. gratings) or interferometers has already been considered for possible frequency tuning. v) The long resonator length also permits the control of the longitudinal mode spacings to favour the fabrication of integrated phase modulators suitable for phaselocking or other applications (see below). This short list of attractive performance features alone warrants a research and development effort.

Figure 6 is a photomicrograph of an active oxide stripe defined gain-guided amplifier ($Al_{0.05}Ga_{0.95}As$) taper coupled to a passive monomode waveguide. The demarcation between the active and passive section is clearly visible in the center. To also permit good lateral mode selection, a multimode passive rib waveguide is coupled to the monomode waveguide via a lateral taper. The rib waveguide is clearly visible in Fig.6, and it is about 5 μm wide and 1mm long. The full length of the passive section is not shown to provide a better resolution of the taper zone. Only the rib waveguide near the center was connected to the amplifier part. The separation between passive rib waveguides is 50 μm. Part of the oxide stripe definition can be seen near the cleaved active mirror.

The nearfield pattern of the modes as observed through an infrared image converter are shown just outside of the active and passive regions. They clearly demonstrate that this device operates as a mode selector and transformer. As the oxide confinement was not very effective, the active nearfield emission is quite large (~ 15 μm) and thus poorly matched to the passive rib waveguide.

Taper coupled structures of a simpler design were operated CW with good frequency and mode stability provided they contained a sufficiently strong lateral guide in the passive section. Devices with no lateral guiding were also fabricated and operated CW. They were very instable and showed very strong kinks in the light vs. current characteristics. The stabilizing properties of passive lateral waveguide are thus clearly demonstrated.[7]

3.3. INTRACAVITY FREQUENCY MODULATION

This integrated device consists of an intracavity arrangement of an optical amplifying and a phase modulator section. Figure 7 shows a schematic cross-section of the amplifier and phase modulator. Feedback is obtained by the cleaved mirrors. Modulator and amplifier are electrically isolated by a groove etched between them. Light emission and gain is provided through the amplifier section. The guided wave modulator serves to adjust the round trip phase of the light by means of the linear electrooptic effect. The oscillation is maintained by the frequency adjustment of the emission to provide for a zero net phase variation. The combination of phase modulation with an optical amplifier thus can result in a true frequency tunable device (without an undesirable amplitude modulation composant). The tuning range is limited by the relative modulator phase

variation $\delta n/n_e$, where δn equals the variation due to the Pockels effect and n_e is the effective group index of the modulator waveguide. The maximum value for the optical wavelength variation is $\delta\lambda = \delta n_{e\,max}$. Values of $\delta n/n_e \sim 10^{-4}$ are readily achieved. A prototype device with dimensions given by Fig. 7 has confirmed these expectations.[8]

Applications of this integrated structure could be varied : (i) Stabilisation of the laser emission for frequency and amplitude; (ii) Laser frequency modulation; (iii) Laser amplitude modulation and (iv) Controlled mode locking for fast pulse generation. The first two applications are self-evident and will not be discussed any further. The laser amplitude modulation (iii) could be achieved by passing the frequency modulated light through an adequate frequency discriminator. Figure 8 represents such a modulation scheme when using a spectrometer of 0.1 Å resolution. A variation of the modulator bias of ± 1.5 V results in a modulation depth of 90 %. This would in principal permit very fast modulation with switching energies less than 1 pJ. As high quality waveguide filters are practical, we could replace the spectrometer by an integrated λ-filter. Phase locking (iv) is commonly recognized as a powerful means to generate ultrashort pulses. The large gain bandwidth of a laser could permit pulse durations as short as a few tens of femtoseconds. Nonlinear and dispersion effects could, however, lead to a large reduction of the useful gain bandwidth. But a conservative estimation indicates the feasibility of pulse durations under 1 ps. The advantage of an active mode locking scheme over the previously demonstrated saturable absorption method will primarly lie in the increased reliability. Considerable research will though be necessary to demonstrate this pulse generation technique.

3.4. PLANAR LASER INTEGRATION WITH BRAGG REFLECTORS

The monolithic integration of optical circuit components must be entirely compatible with planar technology. One of the most direct concepts is based on the demonstrated feasibility of growing wafers with distinctly separated active and passive sections. The coupling between these regions is well controllable with the naturally occuring tapering of the layers at their boundaries. The modified crystal growth necessary is probably easier to control than etching and regrowing of large wafer section. To provide the feedback for lasers, DBR appears to be almost ideal, because it can be one of the final processing steps in integrated device fabrication. Accordingly, there will be fewer constraints for DBR than for DFB, where the grating has to be very close to the region of the active zone.

The cross section of the first DBR device is given in Fig. 9. A third order holographic grating with a periodicity $\Lambda = 0.3865$ µm was fabricated on the passive waveguide between two active taper coupled waveguide regions A and B. Cleaved mirrors in the active region as indicated in Fig. 9 and the grating provided feedback for laser operation of either laser A or B. In a typical operation mode, current would be applied to section A. The unpumped section B served as a termination and guaranteed minimum feedback from its mirrors. Laser action was observed for a current density $j \geq$ kA/cm^2. A very narrow emission spectrum which is reproduced by Fig. 10, was observed with a current density of 6 kA/cm^2. This result indicates a full bandwidth of the DBR laser near 1 Å. The bandwidth of the dominant modes at the half power points taken from Fig. 10 is 0.2 Å. The fine structure of the spectrum probably was caused by a number of longitudinal and lateral modes that coexisted in this broad area device.

The structure of Fig. 9 provides for the possibility of operating the second section as a detector or a laser amplifier. This implicit integration level was not demonstrated as the long grating length (1,5 mm) and the relatively high loss of the passive waveguide (20 cm^{-1}) prevented useful coupling to section B. Better control of the crystal growth and all the processing parameters will eventually permit a multicomponent integration in the future.

VIII. CONCLUSIONS

The examples given above outline the feasibility of a monolithic optical integration approach. The controlled growth of the basic crystal layers to form desired patterns emerges as the most crucial topic; but the processing and assembly technologies are also of great importance. Trade off between the complexities of the crystal growth steps, the processing technologies and the design is possible to a certain extent. As layer dimensions, composition and doping level tolerances can be reduced, the greater the design flexibility will be. This is illustrated by the case of taper coupling between modes of different layers : the precise shape of the taper is not important for efficient coupling as long as it is smooth, several µm long, and its fabrication does not result in any new defects. Actual and anticipated system requirement permit a varying level of escalating complexities that can already be identified. Research directed at fundamental problems (e.g. quantum wells, superlattices and quantum effects) may provide the clues to their resolution.

Research and development in the technological domain is likely to fertilize systems and fundamental aspects. With no universal solution in

sight we must not loose sight of the practical implications imposed by them to meet the challenge.

The author would like to thank Mlle V. Mercier for the preparation of the manuscript.

TABLE I

DEVICE COMPONENTS FOR INTEGRATED OPTICS

SOURCES	DETECTORS	WAVEGUIDES	MODULATORS / SWITCHES		ELECTRONIC
LED	p-n	TWO-DIM.WG: MM,SM	PHASE	CUT OFF	IMPATT
	p-i-n	TAPER (MM-SM)	POLARIZATION		
LASER	APD	OFFSET/BENDS		COBRA	GUNN
(CLEAVED)	SCHOTTKY	REFLECTORS			
(ETCHED)		POL. FILTER	ELECTROAB-SORPTION		
(MESA)	PHOTOCONDUCTOR	λ-FILTER		STEP Δβ REV.	BIPOLAR TRANSISTOR
(DFB/DBR)		BRANCH COUPLER			
		PHASE COUPLER	p-n		
ARRAYS		STAR COUPLER		MATRICES 8x8	FET
	PYROELECTRIC		SCHOTTKY		
			HETEROJCT.		VARACTOR
			MOS		

TABLE II : REQUIREMENTS FOR OPTICAL WAVEGUIDE DEVICES FOR MONOLITHIC OPTICAL INTEGRATION

The parameter $\Delta = 1 - n_c^2/n^2$ measures the strength of the optical waveguide. The optical dielectric constants of the waveguide and cladding are n^2 and n_c^2 respectively.

COMPONENT	Δ	SCATTERING LOSS	REMARKS	CURRENT DENSITY
passive WG	10^{-3} - 10^{-1}	very low $< 1\ cm^{-1}$	$\omega \ll E_g$	—
Modulator	same	E.A. $< 3\ cm^{-1}$	$\omega < E_g$	low
		P.M. switches $< 1\ cm^{-1}$	$\omega \ll E_g$	—
Laser Amplifier	$\leq 10^{-1}$	$\leq 20\ cm^{-1}$	$\omega \simeq E_g$	$10^3\ A/cm^2$

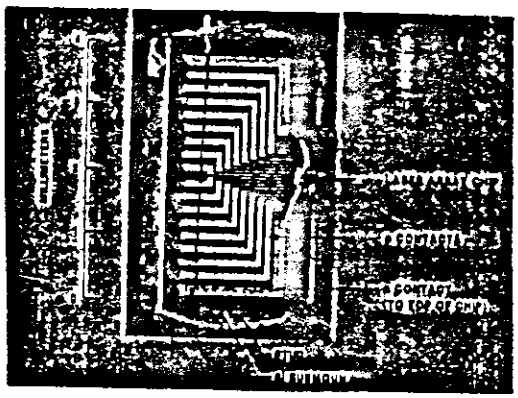

FIG. 1 Contact arrangement of a laser array.

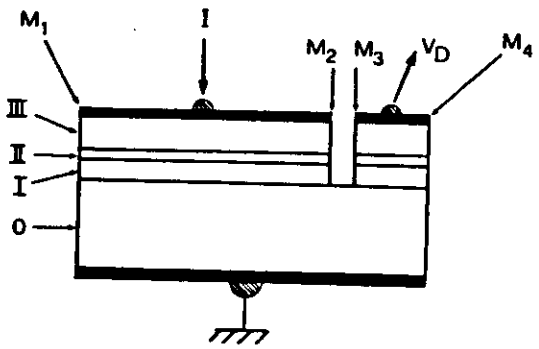

FIG. 2 Integrated laser - detector with etched mirrors

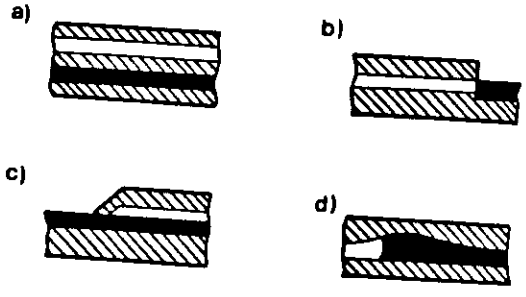

FIG. 3 Integration possibilities.

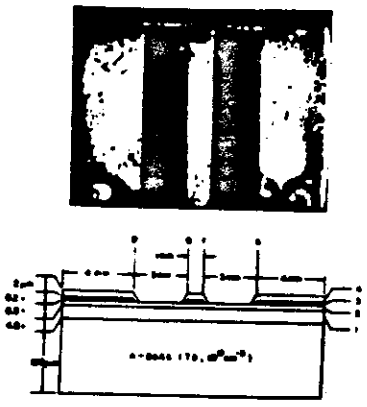

FIG. 4 Laterally structured layer for integration. Top: Photoluminescence.

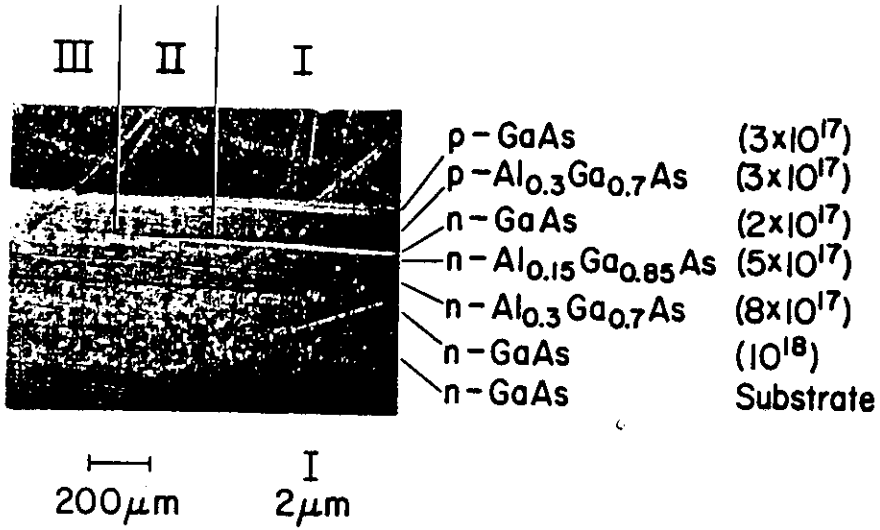

FIG. 5 Tapered GaAs layer grown by MBE for optical integration.

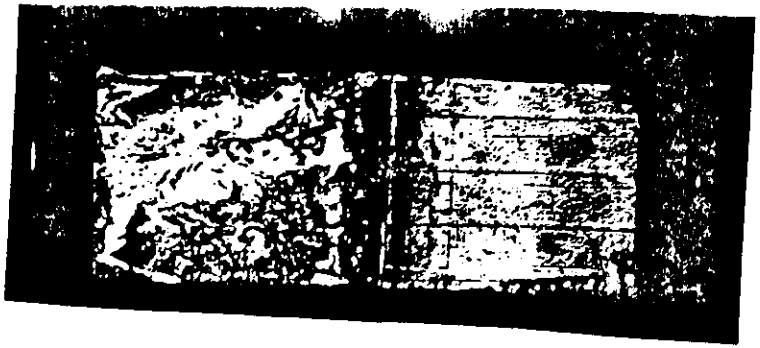

FIG. 6 Taper coupled laser with lateral mode confinement.

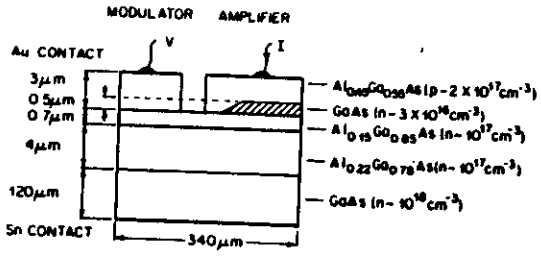

FIG. 7 Integrated Phasemodulator.

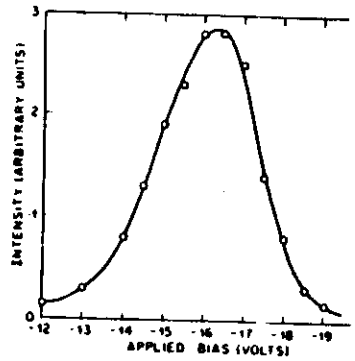

FIG. 8 FM - AM conversion.

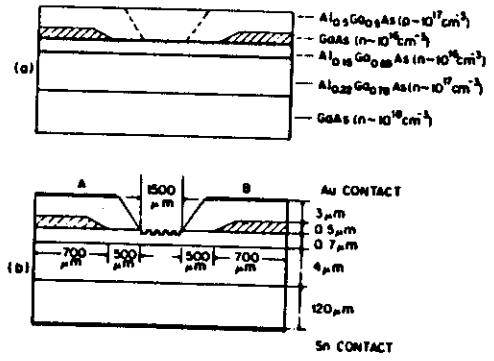

Fig. 9 Laser with DBR grating. a) Composition distribution. b) Dimensions.

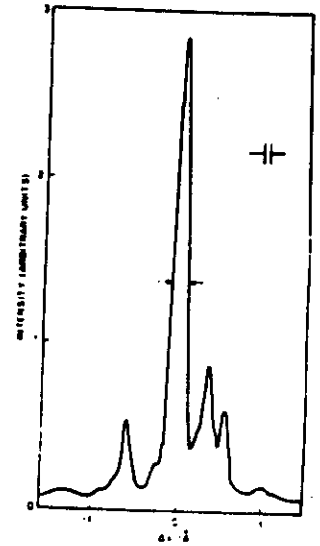

FIG. 10 Spectrum of DBR laser.

REFERENCES (SECTION VII)

1. H. Nakano, S. Yamashita, T.P. Tanaka, M. Hirao, and Minoru Maeda, J. Lightwave Tech. LT-4, 574 (1986).

2. W.T. Tsang, N.A. Olson, and R.A. Logan, Appl. Phys. Lett. 42, 650 (1983).

3. K.H. Zschauer, (3 Laterally Coupled Laser WG) Private Communication (1985). R.J. Lang, J. Salzman, and A. Yariv, Integrated and Guided Wave Optics, Tech. Digest FBB5, Atlanta, Georgia, 26-28 Feb. 1986.

4. Y. Tohomori, K. Komori, S. Arai, Y. Suematsu, and H. Ooashi , Integrated and Guided Wave Optics, Tech. Digest FBB4, Atlanta, Georgia, 26-28 Feb.1986.

5. Ref. 16. Section VI.

6. F.K. Reinhart and A.Y. Cho, Appl. Phys, Lett. 31, 459 (1977).

7. F.K. Reinhart, R.P. Salathé, R.A. Logan, R.L. Hartman, L.A. Koszi, and G. Badertscher, Topical Meeting on Integrated and Guided Wave Optics, Post Deadline Paper, Salt Lake City, Utah, 16-18 Jan. (1978).

8. F.K. Reinhart and R.A. Logan, Appl. Phys. Lett. 27, 532 (1975).

9. F.K. Reinhart, R.A. Logan, and C.V. Shank, Appl. Phys. Lett. 27, 45 (1975).

SUPERLATTICE p-i-n WAVEGUIDE DEMULTIPLEXER

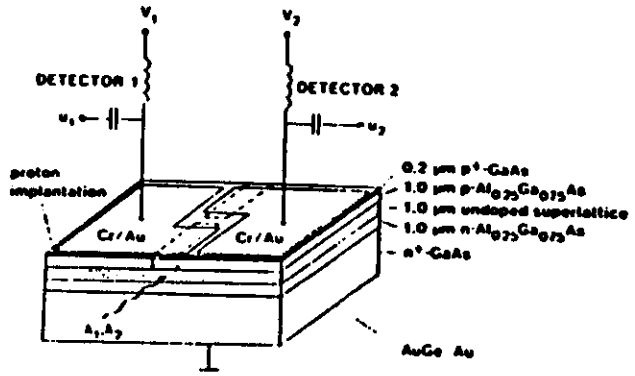

FIG. 1 Schematic view of the two-wavelength demultiplexing superlattice *p-i-n* waveguide detector. The superlattice consists of 100-Å GaAs wells and 50-Å $Al_xGa_{1-x}As$ barriers and is surrounded by undoped graded superlattice buffers, each with a total thickness of 385 Å. The detectors are 20 μm wide, the lengths of detectors 1 and 2 are 20 and 50 μm, respectively, and the separation is 10 μm.

A. LARSSON, P.A. ANDREKSON, P. ANDERSSON, S.T. EVG

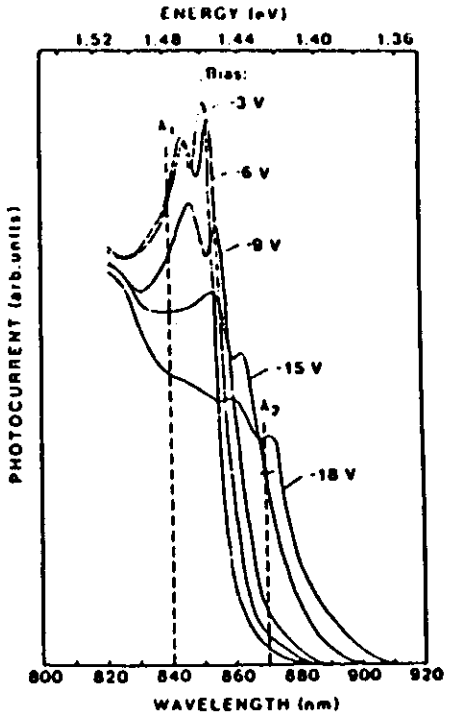

FIG. 2. Photocurrent spectra under different applied reverse biases. The dashed lines indicate the wavelengths (λ_1 and λ_2) used in the demultiplexing experiment

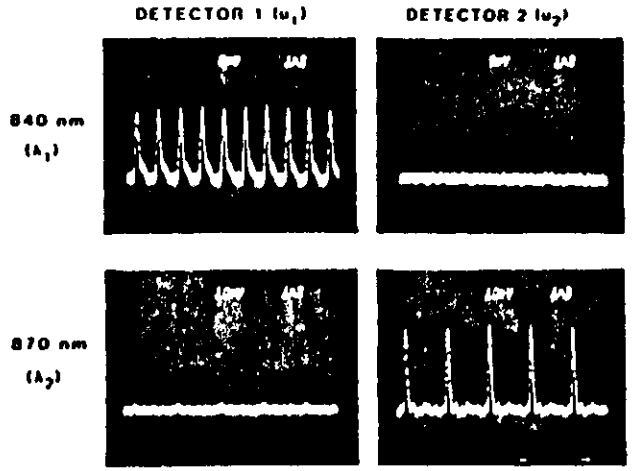

FIG. 4. Results of the dual-wavelength demultipleaing experiment. Detector 1 and detector 2 were reverse biased at 5 V (V_1) and 15 V (V_2), respectively.

Siemens Forsch.- u. Entwickl.-Ber. Bd. 14 (1985) Nr. 6

Monolithic Phase-Locked GaAlAs Laser Arrays

F. Kappeler

0 Introduction

The high structural and compositional uniformity of epitaxial layers grown by recently developed methods allows the integration on one and the same substrate of a large number of semiconductor lasers arranged side by side. The original objective of this effort was to obtain higher power levels in a stable radiation pattern than those available from a single laser [1–3]. The lateral optical coupling of closely spaced laser resonators provides however certain additional features such as phase-locked operation and longitudinal mode selection [4, 5]. These valuable features open up a wide range of applications for optically coupled laser arrays in both the classical field of high-power lasers and the field of optical communication, where information has to be distributed and transmitted at high bit rates.

The purpose of this report is to survey the design, performance and applications of various types of GaAlAs laser arrays recently developed at our laboratories. A short discussion of the basic coupling effects will be followed by descriptions of three types of laterally coupled multiple-stripe laser devices:

(a) high-power laser arrays,
(b) arrays with a controllable radiation pattern,
(c) dynamic single-mode laser arrays.

Special attention is devoted to the laterally coupled waveguide (LCW) laser, a novel triple-stripe structure offering attractive features for optical transmission at high bit rates in long-haul optical communication systems.

1 Coupling Effects

Figure 1 shows a schematic view of an array of five gain-guided lasers. In the transverse direction the electric carriers are confined and the optical wave is guided by either a conventional double-heterostructure (DH) with a 100 nm thick active layer or by a multiple quantum well (MQW) structure [6], both grown by metal-organic vapor phase epitaxy (MO VPE) [7]. In the latter case the active layer is divided into a number of extremely thin sublayers with different band gaps. The potential wells thus formed help to improve the optical coupling between neighboring laser channels.

Optical coupling in the lateral direction takes place when the individual laser stripes are arranged so close together that their lateral field profiles overlap. Consequently the coupling efficiency should increase with decreasing center-to-center spacing D. Lateral optical coupling produces two main effects:

One is that the optical loss between the laser stripes is drastically reduced due to the electrical and optical pumping from adjacent emitters. This effect reduces the threshold current per stripe and improves the differential efficiency as a function of the center-to-center spacing D. As shown in Figure 2, the pulsed threshold current per stripe of DH arrays decreases from 100 mA, which is almost the threshold of a single-stripe laser, to about 30 mA as D is reduced from 40 µm to 8 µm. Still lower values of 22 mA per stripe were achieved with MQW arrays. At the same time the differential efficiency per facet increases up to 0.4 W/A for DH arrays and up to 0.55 W/A for MQW arrays. Thus the reduction of the optical loss considerably improves the power conversion efficiency of a laser array over that of a single laser.

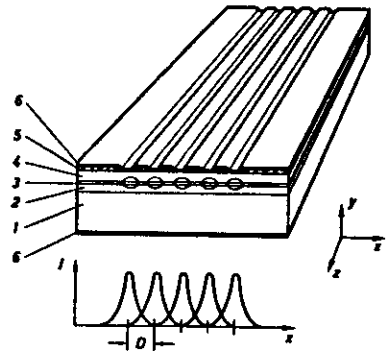

Figure 1. Schematic view of an array of five gain-guided oxide stripe lasers with overlapping lateral intensity profiles $I(x)$. *1* Substrate, *2* and *4* Cladding layers, *3* Active layer, *5* Oxide isolation, *6* Metal contacts, D Center-to-center spacing

Manuscript received on September 5, 1985

Dr.-Ing. Franz Kappeler, München
Siemens AG, Forschungslaboratorien

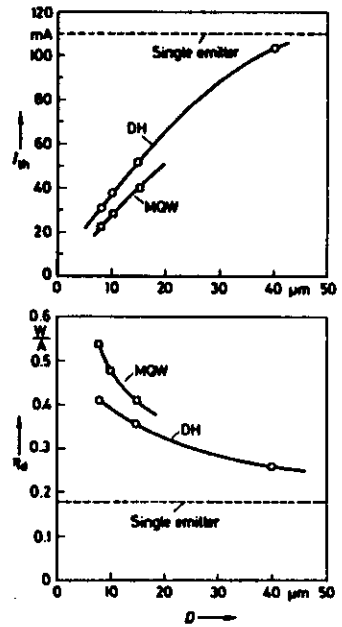

Figure 2. Threshold current I_{th} per stripe and differential efficiency η_d of DH and MQW arrays versus the center-to-center spacing D

The other effect of lateral optical coupling is the phase-locked operation of the individual emitters of an array. Similarly to a system of coupled oscillators, an array of N coupled lasers has N allowed eigenoscillations known as supermodes. In each supermode the array elements oscillate in synchronism at a specific frequency with a specific spatial distribution of their amplitudes and relative phases [8, 9]. Figure 3 shows for example the supermode patterns of a 5-stripe array calculated analytically [11] for the simplified case of plane-wave emission. It is evident from Figure 3a that $k-1$ sign reversals and k intensity maxima occur in the kth supermode, leading to in-phase operation of all emitters in the fundamental mode and to 180° out-of-phase operation in the highest-order supermode. The phase shifts of the near fields greatly influence the corresponding far-field patterns (Figure 3b).

Whereas only the fundamental supermode radiates in a single lobe, the far fields of the higher-order modes are split into two main lobes whose angular distance increases with rising mode number. The width of the lobe itself depends on the effective array aperture, reaching the diffraction limit in the ideal case of plane waves.

Of the N allowed supermodes only the one with maximum modal gain will oscillate, i.e. the mode having the best overlap with the gain profile induced by the injected charge carriers. In an array of uniformly spaced emitters, usually the highest-order supermode is preferred [8, 9]. It is alternatively possible, however, to select the fundamental supermode by appropriately choosing the gain profile via the geometry of the coupled emitters [10, 11]. Due to the quenching of some emitters the intermediate

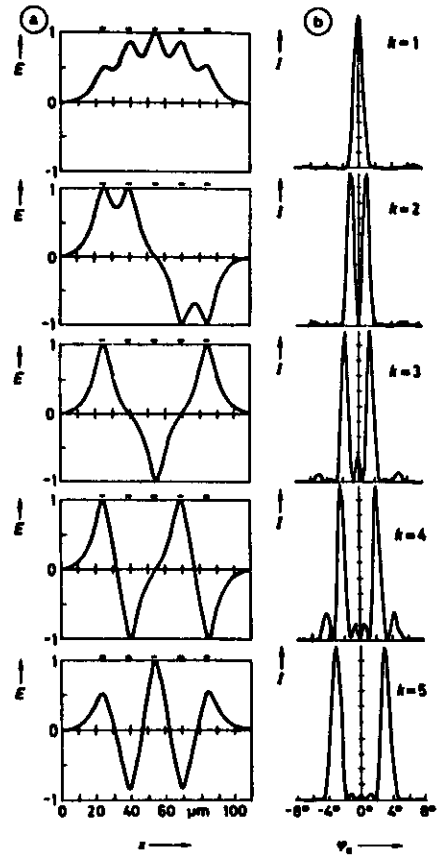

Figure 3. Calculated supermodes of an idealized laser array with 5 stripes on 15 µm centers. (a) Near-field patterns: electric field strength E versus the lateral distance x, (b) Lateral far-field patterns: intensity I versus the lateral angle φ_x. k Order of supermodes

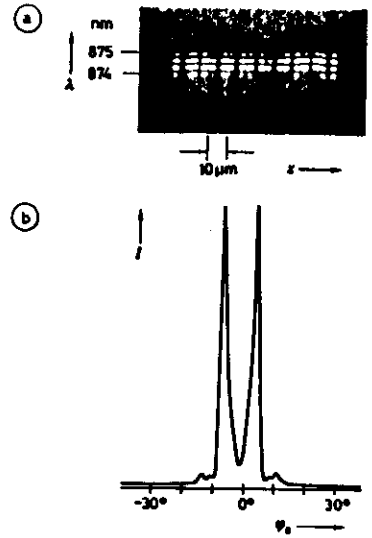

Figure 4. Spectrally resolved near field (a) and lateral far field (b) of an MQW array with 10 stripes on 10 µm centers (λ wavelength)

supermodes have only a small modal gain, whence they are usually not excited.

Figure 4 demonstrates the phase-locked operation of an implemented 10-stripe MQW array. It will be seen from the spectrally resolved near field (Figure 4a) that all laser elements oscillate in synchronism, having identical spectra of a few longitudinal modes. It should be noted that the spectral width of this phase-locked array is about ten times narrower than that of a single gain-guided laser due to the frequency-selective effect of the lateral optical coupling. The lateral far-field pattern consists of two lobes of less than 2° FWHM. This means that, as expected, the array operates predominantly in the highest-order supermode.

The phase-locked operation discussed above is very useful for applications in which high power and good spectral and spatial coherence are essential.

2 High-Power Laser Arrays

Due to the high uniformity of the epitaxial layers grown by MO VPE it is possible to integrate a large number of phase-locked lasers on one and the same substrate. Figure 5a shows a micrograph of an experimental MQW array consisting of 40 laser stripes on 10 µm centers integrated on a 0.4 mm by 0.5 mm chip. This device reaches a maximum cw output power of 1.65 W per facet for a current of 6.0 A

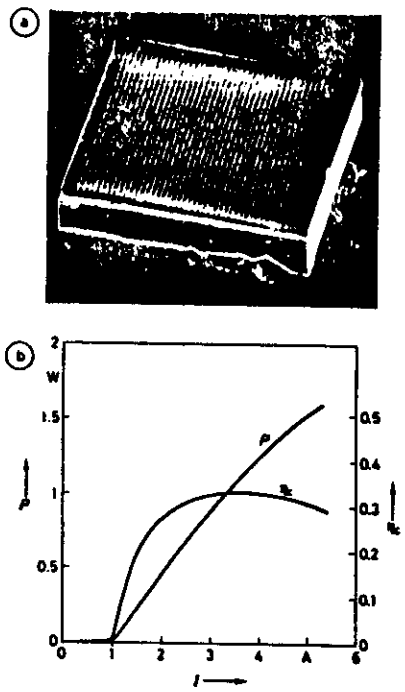

Figure 5. Experimental high-power phase-locked laser array. (a) Scanning electron micrograph of an MQW array chip with 40 laser stripes on 10 µm centers; the chip dimensions are 0.4 mm by 0.5 mm. (b) Output power P per facet and power conversion efficiency η_c versus the driving current I (cw operation, 25 °C)

(Figure 5b). At this power level the facets suffered catastrophic optical damage. The low threshold current (1.0 A or 25 mA per stripe), the high differential efficiency (0.47 W/A per facet) and, above all, the small series resistance (0.1 Ω), contribute to the remarkably high DC-to-light power conversion efficiency (Figure 5b), which reaches a maximum of 33% at an output power of 1.1 W per facet. This good cw conversion efficiency – the highest value reported in recent literature, e.g. [1, 2] – is essential for long high-power laser array lifetime.

12-stripe DH laser arrays with an emission wavelength between 805 nm and 880 nm are currently being produced on a large scale. The arrays are densely packed in long bars cleaved from MO VPE wafers up to 20 mm in length. Typically a bar contains 70 arrays per cm. A 1 µs pulse test of 10 arrays in such a bar distributed across a distance of 14 mm showed all the devices to deliver at least 0.75 W per facet with a standard deviation of less than 5% for both threshold current and differential efficiency

[12]. With 1 µs pulses it is thus possible to obtain from a 1 cm long bar of laser arrays a peak power output of more than 50 W.

One important application of high-power GaAlAs laser arrays is the pumping of Nd:YAG lasers. Since the arrays can be designed to emit at precisely 805 nm – the wavelength of maximum absorption in the YAG material – high overall efficiencies can be realized. Another possible application is the direct optical triggering of high-power thyristors. The optical power of a laser array bar is sufficiently high to allow the simultaneous activation of a group of thyristors over an optical fiber bundle. The good coherence properties of phase-locked laser arrays can further be used to generate coherent blue light (440 nm) by frequency doubling in nonlinear crystals [13].

3 Arrays with a Controllable Radiation Pattern

As discussed in Section 1, a phase-locked laser array oscillating in a selected supermode behaves as a coherent source with a diffraction-limited radiation pattern. This pattern can be controlled by both geometrical means, i.e. by varying the width and center-to-center spacing of the laser stripes, and by electronic means, i.e. by varying the gain and refractive index of the laser channels via their operating currents.

Both control mechanisms are demonstrated in Figure 6. Figure 6a shows the radiation pattern of a triple-stripe array with seven almost diffraction-limited lobes with an FWHM of 1.6°.

As evidenced by the existence of a radiation lobe at the 0° position, the array operates in the fundamental supermode. While the angle between the lobes is given by the 15 µm center-to-center spacing of the emitters, the number of lobes is given by the width of the laser stripes. Thus any reduction of the center-to-center spacing and a broadening of the stripewidth will result in an array with a single far-field lobe (single-lobe laser).

Electronic control of the radiation pattern is made possible by providing a separate electrical contact for each laser channel in the array [14]. An example drawn from this group of devices is a twin-stripe array featuring electronic far-field position switching over an angle of 20° [15]. The two far-field positions of this device are shown by Figure 6b. Bistable behavior can be achieved by the extremely close optical coupling of two laser stripes, which however have separate contacts. Switching from one far-field position to the other is triggered by small differential changes in the operating currents around a threshold value. Continuous beam-steering over a narrower angular range as recently demonstrated experimentally in [16] is also possible with this device.

Due to their high beam directivity, high-power single-lobe lasers are planned for free-space optical

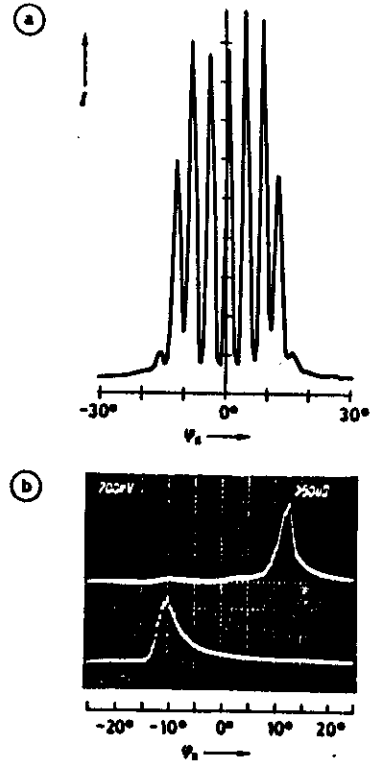

Figure 6. Arrays with controllable radiation pattern. (a) Triple-stripe array with multiple-lobe radiation pattern controlled by the stripe geometry (D = 15 µm). (b) Far field of a bistable twin-stripe array controlled by the operating currents

communication between satellites [17]. Multiple-lobe laser arrays can be used in local-area networks as well as in optical communication systems for the distribution of information among parallel channels. Arrays with a steerable far field hold great promise as fast electrooptical switches for future optical switching matrices and high-speed laser printers.

4 Dynamic Single-Mode Laser Arrays

The frequency-selective effect in laterally coupled lasers offers a new approach to realizing single-mode (or single-frequency) laser sources that exhibit high mode stability even during high-speed large-signal direct modulation. Such laser sources are key elements in long-haul optical communication systems operating at wavelengths of 1.3 µm and 1.55 µm.

Conventional dynamic single-mode lasers such as the distributed feedback (DFB) laser and the cleaved coupled cavity (C^3) laser are stabilized by gratings or multiple Fabry-Perot resonators arranged along the optical axis. These lasers provide effective suppression of unwanted side modes, but show a marked broadening of spectral linewidth of up to several tenths of 1 nm under high-speed direct modulation, e.g. [18, 19]. This chirp effect is caused by periodic changes of the refractive index in time with the modulation current, leading to a modulation of the laser frequency. The transmission range of 1.55 µm optical communication systems is here limited by nonzero dispersion within the optical fiber.

Far higher dynamic mode stability is realized by the lateral coupling of several laser resonators. The laterally coupled ridge waveguide (LCRW) laser [20] consists of three metal-cladded ridge waveguide resonators [21] spaced on 15 µm centers (Figure 7). The central laser is 400 µm in length and has two cleaved facets, while the two side lasers have shorter resonators with one of their facets defined by ion-beam etching [22]. This technique is also used for etching the ridge waveguides and separating the three electrical contact areas. Each of the coupled laser resonators can in this way be biased individually.

For distinct current ratios $I_1:I_2:I_3$ the three lasers synchronize one another and oscillate stably in a single phase-locked mode. Figure 8a shows the static mode spectrum of a tuned LCRW. Due to the additional mode selection provided by the resonators of varying length, the static side-mode suppression ratio (SSR) of this device is as high as 24 dB, which is ten times better than the SSR realized in a device with three resonators of identical length [5]. In dynamic operation the modulation signal is applied only to the central laser. As shown

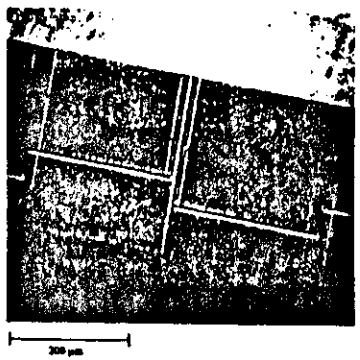

Figure 7. Scanning electron micrograph of an LCRW laser chip with three electrically separated ridge-waveguide lasers of varying length

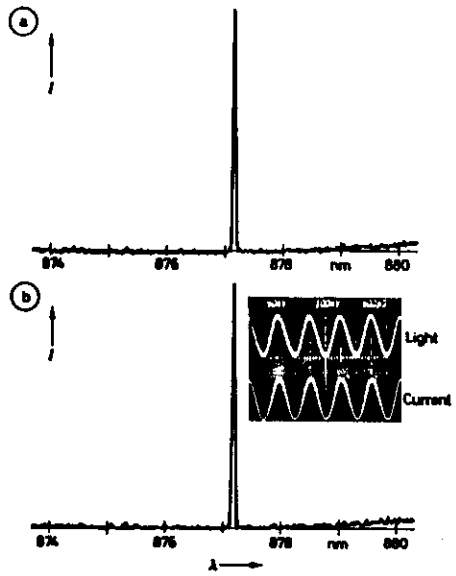

Figure 8. Single longitudinal mode spectra of a phase-locked LCRW laser at 20 mW, 25 °C. (a) Static operation (Side-mode suppression ratio SSR = 24 dB), (b) Modulated at 1.0 GHz with 70 % modulation depth (SSR > 20 dB, chirp ≤ 0.022 nm)

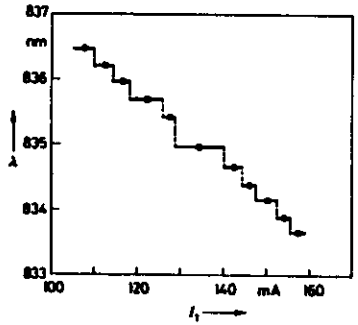

Figure 9. Tuning range of wavelength λ versus the operating current I_1 through a side laser of an oxide-stripe LCW device [5]. I_2, I_3 = const, 25 °C

in Figure 8b, at 1 GHz and 70 % modulation depth the linewidth still retains its static value of 0.022 nm, which is the resolution limit of the monochromator used, with an SSR larger than 20 dB. This chirp is considerably lower than that reported for present C^3 lasers [19] and DFB structures [18], where the

mode broadens up to several tenths of 1 nm for similar drive conditions.

The good dynamic stability of the LCRW laser can be attributed to the fact that a properly tuned device behaves in the manner of a system of three injection-locked oscillators. Since the frequency stability of the two side lasers is not degraded by the modulation current, these reduce the periodic frequency fluctuations of the modulated central laser very effectively as known from injection-locked microwave oscillators [23].

A further advantage of this structure is that the oscillating mode can be tuned via the operating current of one of the side lasers. Figure 9 shows the electronic tuning range of a device with three resonators of identical length [5]. A similar tuning range can be expected for the LCWR laser described above.

5 Concluding Remarks

The basic features of optically coupled multiple-stripe lasers have been discussed and examples given to show how these features can be used in three types of devices.

The reduction of the optical loss leads to very high power conversion efficiencies up to 36 % in high-power arrays with cw output powers of more than 1.5 W per facet. The development of high-power GaAlAs laser arrays grown by MO VPE has matured to the point where fabrication will be possible in the near future.

The radiation pattern of phase-locked laser arrays can be controlled by the emitter geometry as well as via the operating currents as already demonstrated by an array emitting a number of almost diffraction-limited lobes, and by a bistable twin-stripe laser whose far-field positions can be electronically switched over an angle of about 20°.

Finally, a novel dynamic single-mode laser, the LCRW laser, has been developed that, due to its active stabilization by means of two laterally arranged reference lasers, exhibits very limited linewidth broadening (chirp) even under high-speed direct modulation. Because of its simplicity and superior performance as compared to conventional single-mode lasers, an InGaAsP version of the LCRW structure would appear very attractive for high-speed optical communication at a wavelength of 1.55 µm, where chirp is a serious problem.

From the examples cited in this report it can be concluded that the lateral optical coupling of monolithic integrated injection lasers will find widespread use in numerous present and future applications.

The author is indebted to K. Mettler for making this work possible, R. Gessner and M. Druminski for growing the MO VPE wafers, H. Westermeier for preparing the LCRW lasers, J. Luft for preparing and measuring the laser bars and C. Hanke for calculating the supermode patterns.

References

1. Scifres, D.R.; Burnham, R.D.; Lindström, C.; Streifer, W.; Paoli, T.L.: Phase-locked (GaAl)As laser emitting 1.5 W per mirror. Appl. Phys. Letters 42 (1983), pp. 645–647
2. Scifres, D.R.; Lindström, C.; Burnham, R.D.; Streifer, W.; Paoli, T.L.: Phase-locked (GaAl)As laser diode emitting 2.6 W CW from a single mirror. Electronics Letters 19 (1983), pp. 169–171
3. Kappeler, F.; Westermeier, H.; Gessner, R.; Druminski, M.; Zschauer, K.-H.: High cw power array of optically coupled (Ga, Al)As oxide stripe lasers with dc-to-light conversion efficiencies of up to 36 %. 9th IEEE Int. Semiconductor Laser Conf., Rio de Janeiro (1984), pp. 90–91
4. Kapon, W.; Katz, J.; Margalit, S.; Yariv, A.: Longitudinal-mode control in integrated semiconductor laser phased arrays by phase-velocity matching. Appl. Phys. Letters 44 (1984), pp. 157–159
5. Kappeler, F.: Dynamic single-frequency low-chirp operation of a laterally coupled waveguide (LCW) laser. Electronics Letters 20 (1984), pp. 1040–1041
6. Tsang, W.T.: Extremely low threshold (AlGa)As modified multiquantum well heterostructure lasers grown by molecular beam epitaxy. Appl. Phys. Letters 39 (1981), pp. 785–787
7. Druminski, M.; Gessner, R.; Kappeler, F.; Westermeier, H.; Wolf, H.-D.; Zschauer, K.-H.: MO VPE (Al,Ga)As/GaAs 870 nm oxide stripe lasers with highly uniform laser characteristics. Publication pending in Jap. J. of Appl. Phys.
8. Kapon, E.; Katz, J.; Yariv, A.: Supermode analysis of phase-locked arrays of semiconductor lasers. Optics Letters 10 (1984), pp. 125–127
9. Butler, J.K.; Ackley, D.A.; Ettenberg, M.: Coupled-mode analysis of gain and wavelength oscillation characteristics of diode laser phased arrays. IEEE J. QE 21 (1985), pp. 458–464
10. Streifer, W.; Hardy, A.; Burnham, R.D.: Single-lobe phased-array diode lasers. Electronics Letters 21 (1985), pp. 118–119
11. Hanke, C.; Kuppeler, F.; Siegmüller, B.: Influence of waveguiding mechanism on supermode gain in phase-locked laser arrays. Unpublished report
12. Kappeler, F.; Westermeier, H.; Gessner, R.; Druminski, M.; Hanke, C.; Luft, J.: High CW-power phase-locked semiconductor laser arrays. Proc. 7th Int. Congr. Laser 85 Opto-Elektronik
13. Deserno, U.; Kappeler, F.; Hanke, C.: Coherent blue (440 nm) light source by frequency doubling of an 880 nm high-power phase-locked laser array. Publication pending
14. Katz, J.; Kapon, E.; Lindsey, C.; Margalit, S.; Shreter, U.; Yariv, A.: Phase-locked semiconductor laser array with separate contacts. Appl. Phys. Letters 43 (1983), pp. 521–523
15. Kappeler, F.: Continuous and bistable beamsteering in a closely coupled twin-stripe laser. Publication pending
16. Scifres, D.R.; Streifer, W.; Burnham, R.D.: Beam scanning with twin-stripe injection laser. Appl. Phys. Letters 33 (1978), pp. 702–704
17. Katz, J.: Semiconductor optoelectronic devices for free-space optical communications. IEEE Commun. Magazine (Sept. 1983), pp. 20–27
18. Yoshikumi, Y.; Matsuoka, T.; Motosugi, G.; Yamanaka, N.: Fine structures in the broadened line of distributed feedback lasers under high-speed direct modulation. Appl. Phys. Letters 45 (1984), pp. 820–822
19. Agrawal, G.P.; Olsen, N.A.; Dutta, N.K.: Reduced chirping in coupled-cavity-semiconductor lasers. Appl. Phys. Letters 45 (1984), pp. 119–121
20. Kappeler, F.: Improved dynamic single-frequency low-chirp operation of a laterally coupled ridge waveguide (LCRW) laser. IOOC/ECOC 85, Venice, Oct. 1–4, 1985
21. Amann, M.-C.: New stripe-geometry laser with simplified fabrication process. Electronics Letters 15 (1979), pp. 441–442
22. Westermeier, H.; Mettler, K.; Zschauer, K.-H.: (Ga, Al)As injection laser with ion-etched mirrors and monolithically integrated detector. ESSDERC '84, Lille 1984, pap. B9 3, p. 366
23. Kurokawa, K.: Injection locking of microwave solid-state oscillators. Proc. of the IEEE 61 (1973), pp. 1386–1409

TOP

DO NOT AFFIX OVERLAYS ALONG THIS SURFACE

VG. NO. VI 2

J.D. Van der Ziel et al. APL

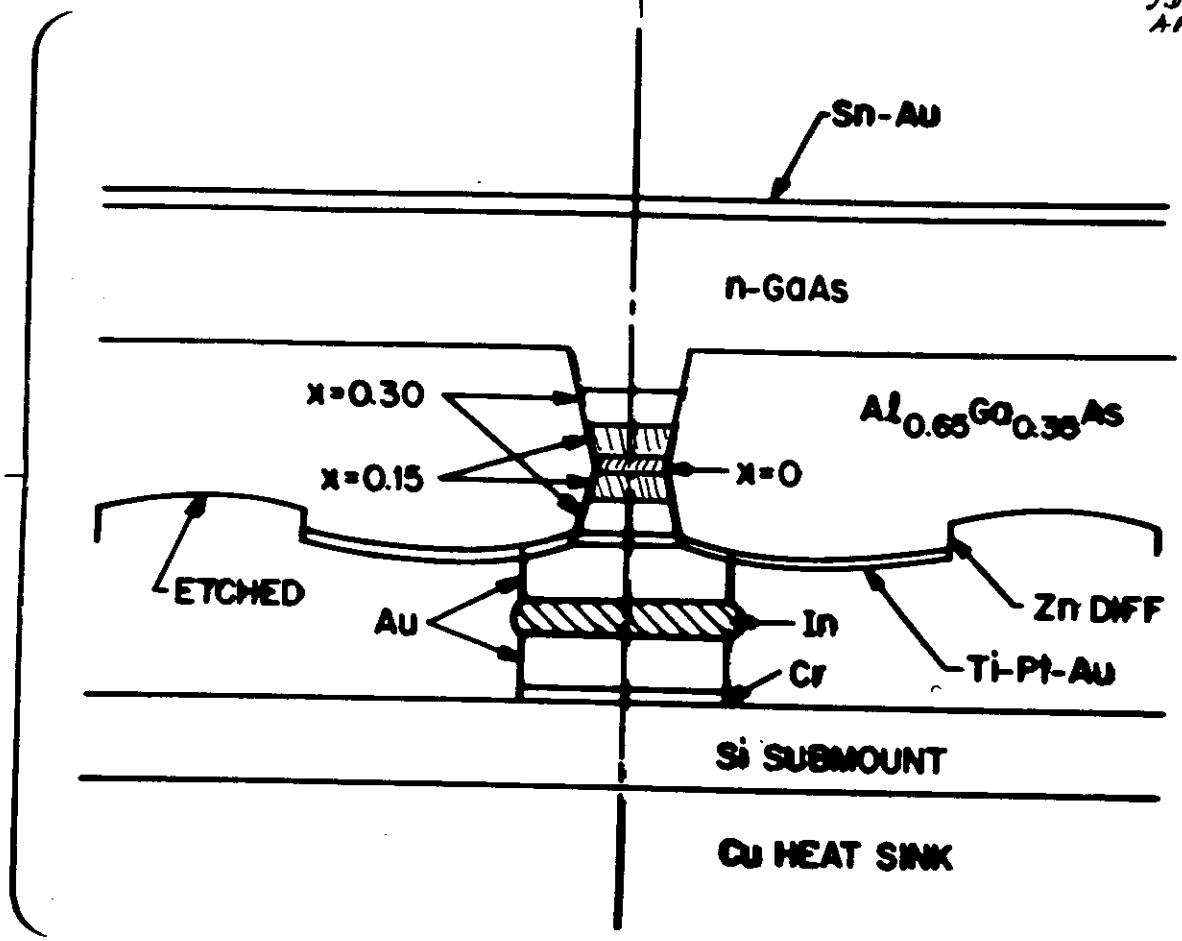

x μm
0.3 1.5 n
0.15 0.5 n
0 0.15 n
0.15 0.5 p
0.3 1.5 p
Zn diff.

$H_2SO_4 : H_2O_2 : H_2O$
1 : 8 : 10

4μm top
0.2μm mesa

$\ell = 250\mu m$
20 Wafers

← Au 3μm
up-plated
← Au ½μm

$I_t \simeq 11$ mA

BH – LASER ARRAY ELEMENT

F-01AR (5-78)

Bell Laboratories

NOTES:

TOP

DO NOT AFFIX OVERLAYS ALONG THIS SURFACE

INDIVIDUALLY ADDRESSABLE LASER ARRAY

16 DIODES
50μm
Center-center
possibility
to reduce
to 15μm c-c

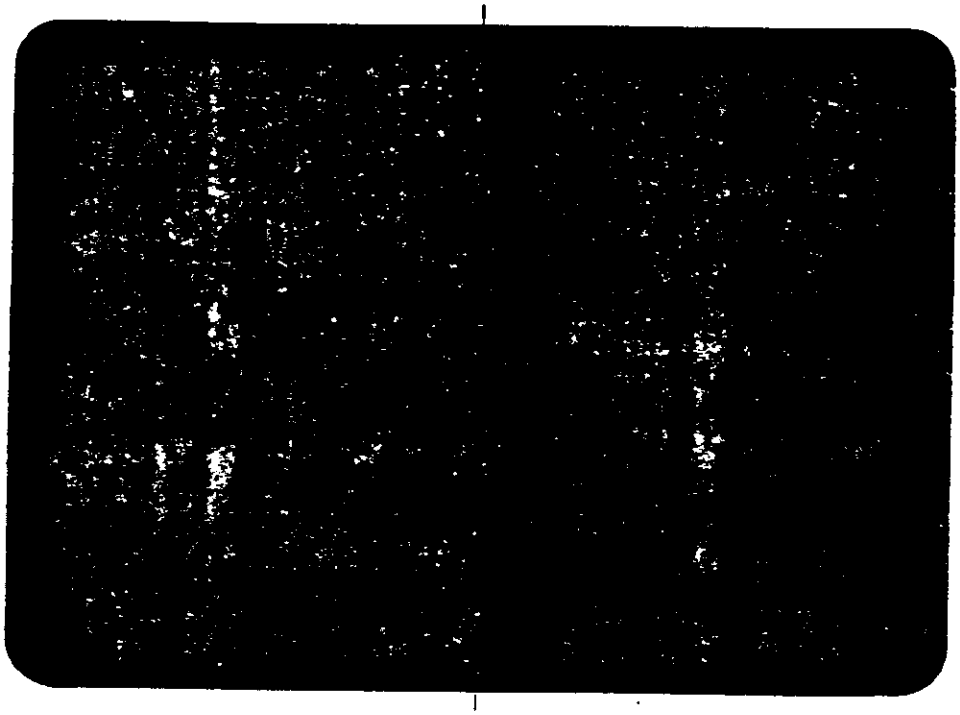

Bell Laboratories

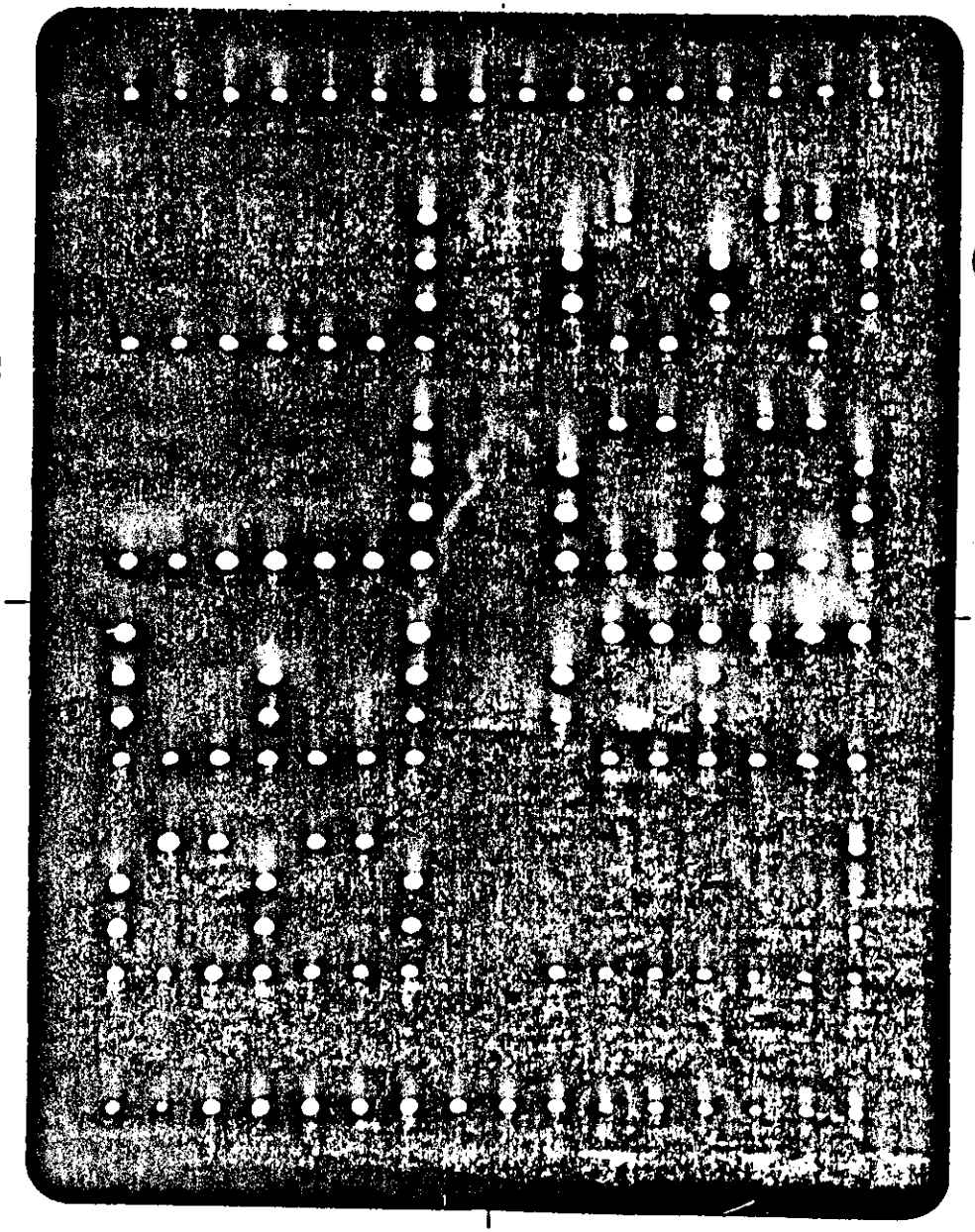

Siemens Forsch.- u. Entwickl.-Ber. Bd. 14 (1985) Nr. 6

1.3 µm Surface-Emitting (In, Ga) (As, P)/InP LED for Transmission Rates up to 200 Mbit/s

H. Albrecht, L. Hoffmann, Ch. Lauterbach, M. Plihal, H. Schäfer, M. Schießl

0 Introduction

1.3 µm surface-emitting InGaAsP/InP LEDs are highly reliable and relatively inexpensive light sources for medium-haul optical communication systems [1, 2]. The feasibility, for example, of using such LEDs in conjunction with graded-index multimode fibers for 8 km unrepeatered links operating at 274 Mbit/s [3] and 5 km links operating at 400 Mbit/s [4] has been demonstrated. Surface-emitting LEDs with a very high modulation capability up to 1.6 Gbit/s have also been reported [5]. Even the use of surface-emitting LEDs in conjunction with single-mode fibers was recently considered, although edge-emitting LEDs, which launch higher power into single-mode fibers and feature a narrower spectral linewidth, appear more promising [6, 7] for this application. These may be used instead of laser diodes as long as the latter are not available as highly reliable and inexpensive optical transmitters.

The present report treats the optimization of surface-emitting LEDs for use in conjunction with graded-index fibers. Special emphasis is placed on the assessment of optimized LEDs for graded-index fibers with a core diameter of 63 µm and a numerical aperture of $A_N = 0.29$. Such LEDs will find application in compact and miniaturized optical transmitter modules which, used in conjunction with InGaAs pin photodiodes, will provide data links operating at a transmission rate of 200 Mbit/s over distances between 2 km and 4 km.

1 LED Structure and Fabrication

Figure 1 shows a cross section through the surface-emitting LED used in the reported investigations. The fabrication of such LEDs has been described in detail elsewhere [8]. A double heterostructure consisting of an n–InP buffer layer/p–InGaAsP active layer/p–InP cladding layer is grown by liquid phase epitaxy (LPE) on an n–InP:S substrate [9]. The 4 µm thick n–InP buffer layer is doped with an Sn concentration of $3 \cdot 10^{18}\,cm^{-3}$ and the 1 µm thick p–InP cladding layer with a Zn concentration of $1 \cdot 10^{18}\,cm^{-3}$. For the 1 µm p–InGaAsP active layer the Zn doping concentration was varied between $1 \cdot 10^{18}\,cm^{-3}$ and $8 \cdot 10^{18}\,cm^{-3}$. For a low contact resistance, a p–InGaAsP cap layer (1 µm thick, Zn doping concentration $5 \cdot 10^{18}\,cm^{-3}$) is grown. After an additional p-diffusion this layer is selectively etched to leave a mesa with the same diameter as the p-contact. This is followed by the Ti/Pt/Au vapor deposition of the entire p-contact. These process steps result in a small-area p-contact of low resistance, while in the remaining area of the chip the reverse-biased Schottky contact

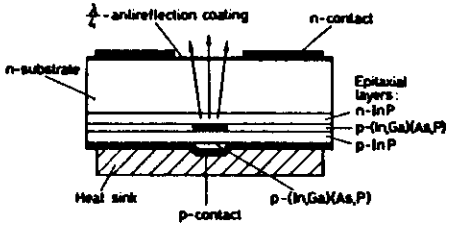

Figure 1. Cross section through an (In, Ga) (As, P)/InP LED

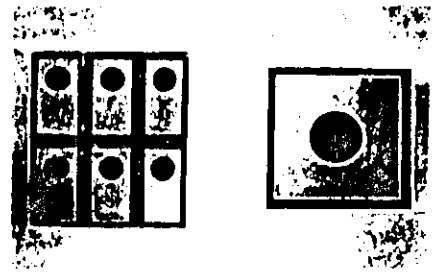

Figure 2. Plan view of six LED chips (left) as used for the investigation and of a chip with an edge length of 400 µm (right)

Manuscript received on August 14, 1985

Dr.-Ing. Helmut Albrecht, München
Dipl.-Phys. Dr. rer. nat. Ludwig Hoffmann, München
Christl Lauterbach, München
Dipl.-Phys. Dr. rer. nat. Manfred Plihal, München
Dipl.-Phys. Dr. rer. nat. Herbert Schäfer, München
Dipl.-Ing. Monika Schießl, München
Siemens AG, Forschungslaboratorien

ACCEPTED
IGWO 28-30 March
STA. FE, NM.

Room temperature c.w. GaAs surface-emitting laser with integrated Bragg reflector

J.Faist, F.Morier-Genoud, D. Martin, J.D.Ganiere, F.-K. Reinhart

Institut de Micro et Optoélectonique, Departement de Physique,
Ecole Polytechnique Fédérale de Lausanne,
1015 Lausanne, Switzerland

Abstract:
Room temperature c.w. operation of an optically pumped surface-emitting laser with GaAs active layer and two Bragg AlAs/$(AlAs)_2(GaAs)_9$ reflectors is reported. Threshold pump power of 16mW, and quantum efficiencies up to 7% are demonstrated.

Introduction. The surface emitting laser [1,2] is expected to revolutionize semiconductor laser array technology. It will permit to reduce beam divergence and increase the emitted power through utilisation of a larger aera of the wafer. The ultrashort cavity also provides for essentially single longitudinal mode operation. It was shown recently that Fabry-Perot resonators with all-dielectric mirrors can be grown [3,4], and that these structures can lase when photopumped [5]. Similar structures can also be used for efficient photonic switching. In this paper, we demonstrate the first low threshold photopumped surface-emmiting laser that operates c.w. at room temperature.

Experiment. The structure was grown by molecular beam epitaxy on a (001) oriented Si doped GaAs substrate at 680°C. The 1.8µm thick GaAs active layer is sandwiched between two identical Bragg reflectors formed with quarter-wave AlAs and $(GaAs)_9(AlAs)_2$ superlattice layers.The theoretical reflectivity of 20 quarter-wave pairs is 99.3%. The use of superlattices instead of $Al_xGa_{1-x}As$ permits us to keep the temperature of the Al oven constant through the whole growth, thus greatly improving the regularity of the layer. The scanning electron micrograph of Fig.1 shows the layer sequence.The room temperature photoluminescence of the superlattice peaks at 778nm.

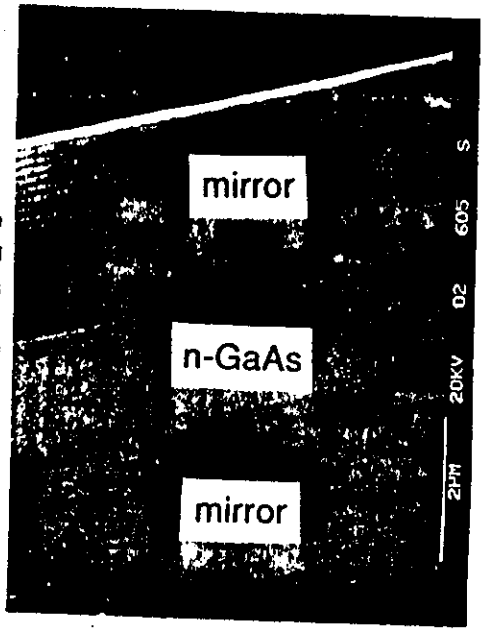

Fig .1 Scanning electron micrograph of the structure. The lightly doped ($n=10^{16}cm^{-3}$) GaAs active layer is surrounded by the two Bragg reflectors each consisting of 20 pairs of 740Å AlAs and of 630Å superlattice layers. The superlattice itself is formed by 20 pairs of 2 monolayers of AlAs and 9 monolayers of GaAs. Long range thickness variation are ±10% over the 2" wafer.

Result and discussion. The mirror reflectivity was checked in the 700-1200 nm range with a Beckmann Spectrophotometer. The position of the stop band of 80 nm width varied from 730 nm to 900nm due to long range thickness variation on the 2" wafer. The mirror reflectivity deduced from these measurements is > 97 %. The regions that demonstrate lasing have the stop band centered from 870 to 900 nm. For these structures, the reflectivity falls to less than 15 % in the 810-830 nm range. We tune the Styril 9M c.w. dye laser to pump the structure at this minimum of reflectivity. The light is focused on an area of 20-50 μm^2 with a microscope objective to produce c.w. lasing without the need of heat sinking. The lasing wavelength varies from 870 to 908 nm depending on the position of the spot on the wafer. The lowest threshold power of 16 mW is obtained at 880 nm. This corresponds to an estimated pump density of $8x10^4 W/cm^2$ and yields an equivalent threshold current of 11 mA. The carrier concentration is more difficult to estimate, due to the ambipolar lateral diffusion of the carriers. Our estimation, based on threshold measurement for different spot sizes, gives the approximate value of 2×10^{18} cm^{-3}. From the reflectivity measurements and the active layer thickness we estimate a gain of ≤ 200 cm^{-1}. This value is only a factor of 4 above that of a conventional laser, and it is well within the range of our estimated carrier density using the GHLBT-SME model [6]. However, the threshold power and the lasing wavelength are very dependent on the position of the pump spot. This is attributed to a slight layer roughness of ± 100 Å on a 0.5 µm distance.The lasing versus pump power characteristic of Fig.2 shows a sharp threshold and a linear relation above threshold. The differential quantum efficiency varies from 1 to 7%. The discrepancy between these values and the theorical value of 90% obtained from assumed cavity losses of 20 cm^{-1} and mirror losses of 170 cm^{-1} is attributed to scattering of the light in the mirrors.The linewidth of the laser for different pump power has been measured with a 1-meter spectrometer. Figure 3 gives the spectral output for three different pumping powers.

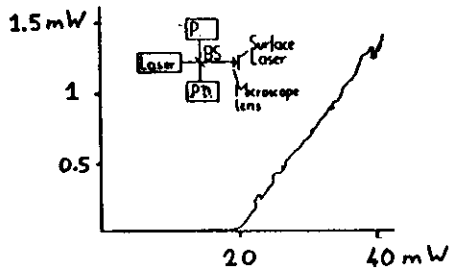

Fig. 2 Lasing power versus pump power. The differential quantum efficiency is 6.5%. The total ouput power is extrapolated from the known losses of the microscope lens and the beam-splitter,and assuming that 50% of the lasing power exits from the upper mirror.

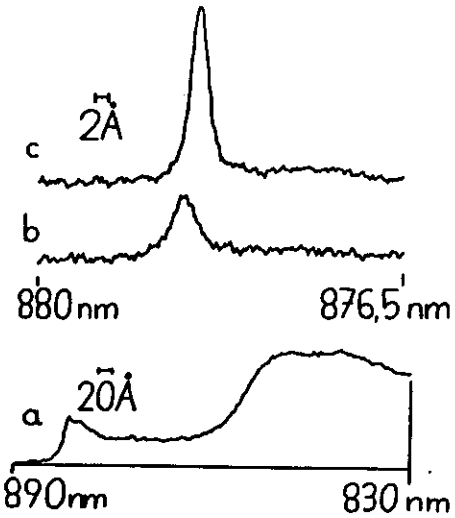

Fig. 3 Light spectra of the laser for three value of the pump power. Resolution is 2Å for a), and 0.2Å for b) and c). Vertical scale is expanded x20 in a). a) Pump power is 7 mW. The depression in the spectrum between 850 and 885 nm is due to the high reflectivity of the mirror. b) Pump power is 16 mW, with a clear onset of lasing. c) Pump power is 18mW, and the laser linewidth is 3Å

The smallest linewidth obtained is 2.7 Å, limited by the length variation of the Fabry-Perot resonator across the lasing spot. High threshold sections usually yield higher linewidth (5-10 Å).

Conclusion. We have demonstrated a surface emitting laser with low threshold, relatively high differential quantum efficiency that operates CW at room temperature. The performances of the structure can be improved by fabricating layers with higher flatness.

Acknowledgement. This work was made possible through grants from the Swiss Federal Postal Administration (GD-PTT) and benefited from a joint program with Thomson CSF. The authors want to thank M.Berz and Dr. D. Pavuna for stimulating discussions and help in evaluation.

Bibliography.

[1] S.Kinoshita, T.Odagawa, and K.Iga, Jpn. J.Appl. Phys. 25, 5264 (1986)

[2] K.Iga, S. Kinoshita, and F.Koyan, 10th IEEE International Semiconductor Laser Conference, October 14-17, 1986, Kanazawa, Japan, paper PD-4.

[3] J.P.Van der Ziel and M.Ilegems, Appl.Opt.14, 2627 (1975); 15,1256

[4] P.L.Gourley and T.J.Drummond, Appl.Phys.Lett. 49, 489 (1986)

[5] P.L.Gourley and T.J.Drummond,Appl.Phys.Lett. 50, 1225 (1987)

[6] H.C.Casey and M.B.Panish, Heterostructure Laser, Academic Press,1978

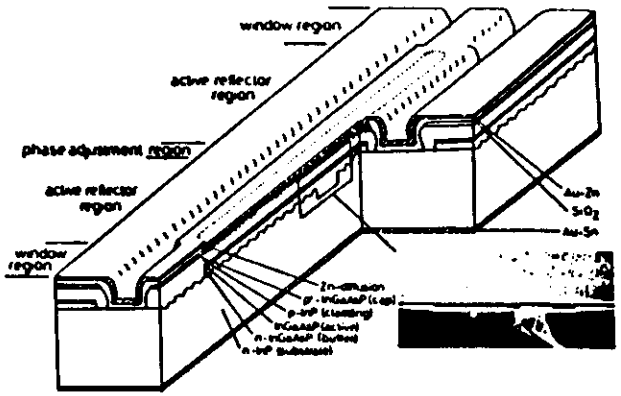

Fig. 1 Cut-away view of the laser. The photograph shows the phase-adjusting groove.

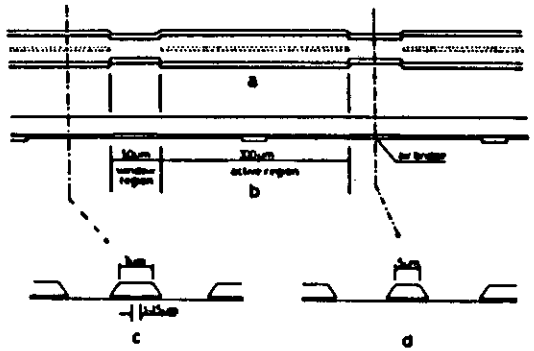

Fig. 2 The laser structure before mass transport: (a) top view, (b) side view of the laser mesa, (c) cross-section active region, (d) cross-section window region.

Fig. 3 (a) Cross-section of active region after mass transport, (b) cross-section of the window region 25 μm from the active region. The sample is stain-etched in the same way as in (a).

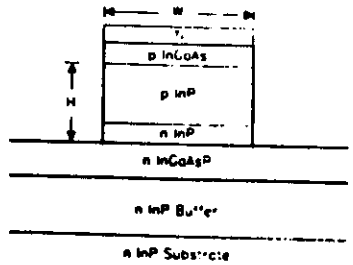

THAA4 Fig. 1. Layer structure of InGaAsP/InP ridge waveguide phase modulator.

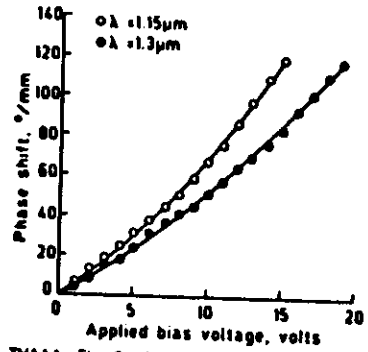

THAA4 Fig. 2. Measured phase change per unit length with applied voltage: rib width $W = 3$ μm at $\lambda = 1.15$ μm; $W = 4$ μm at $\lambda = 1.3$ μm.

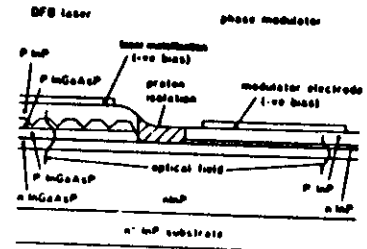

THAA4 Fig 3 Cross section of the layers of a proposed DFB/phase modulator structure

BRODERG ET AL. OFC 85

89

P.M. RODGERS ET AL. BTRL

91

HITACHI CRL, TOKYO

T. FUKUZAWA, M. NAKAMURA
H. HIRAO, T. KURODA, & J. UMEDA
APPL. PHYS. LETT. 36, 151 (1980)

3 μm gate, GaAlAs insulator
$\tau_n, \tau_t < 0.4$ ns
$\ell_{min} = 300$ μm
PIONEERED IN

I. URY, S. MARGALIT, M. YUST
AND A. YARIV APL 34, 430 (1979)

ON SEMIMS. SEMICONDUCTORS

SiO_2 : 0.5 μm

Minimum gate length ~ 1 μm

Normally-off, 0.1 μm FET

MONOLITHIC INTEGRATION OF A LASER AND DRIVING CIRCUITS IN GaAs/GaAlAs SYSTEM FOR HIGH SPEED OPTICAL TRANSMISSION

M. Hirao, S. Yamashita, T.P. Tanaka, H. Nakano

Central Research Laboratory, Hitachi, Ltd., Kokubunji, Tokyo 185, Japan

Fig. 1 Schematic structure of the integrated laser diode

Fig. 2 Diagram of electronic circuit

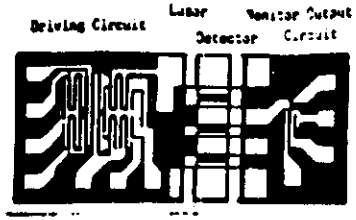

Fig. 3 Photograph of a fabricated OEIC chip

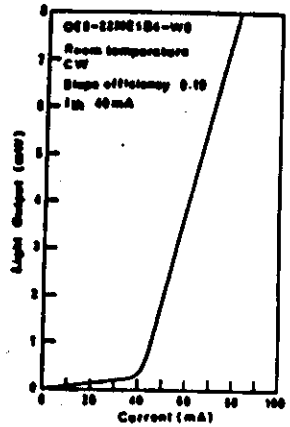

Fig. 4 I-L characteristics of a integrated laser

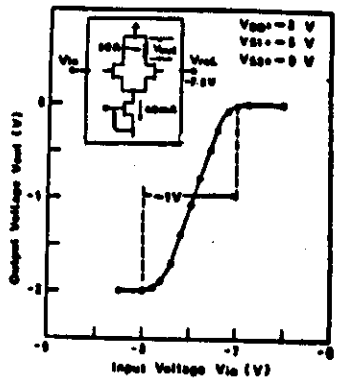

Fig. 6 DC switching characteristics of the electronic circuit

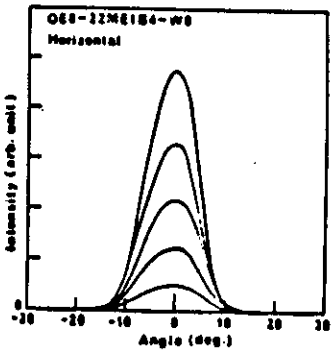

Fig. 5 Far field patterns of a laser parallel to the junction plane

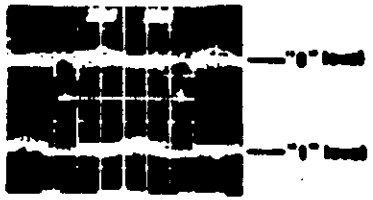

Fig. 7 Eye pattern of the driving circuit

HONEYWELL INTEGRATED LASER DRIVER

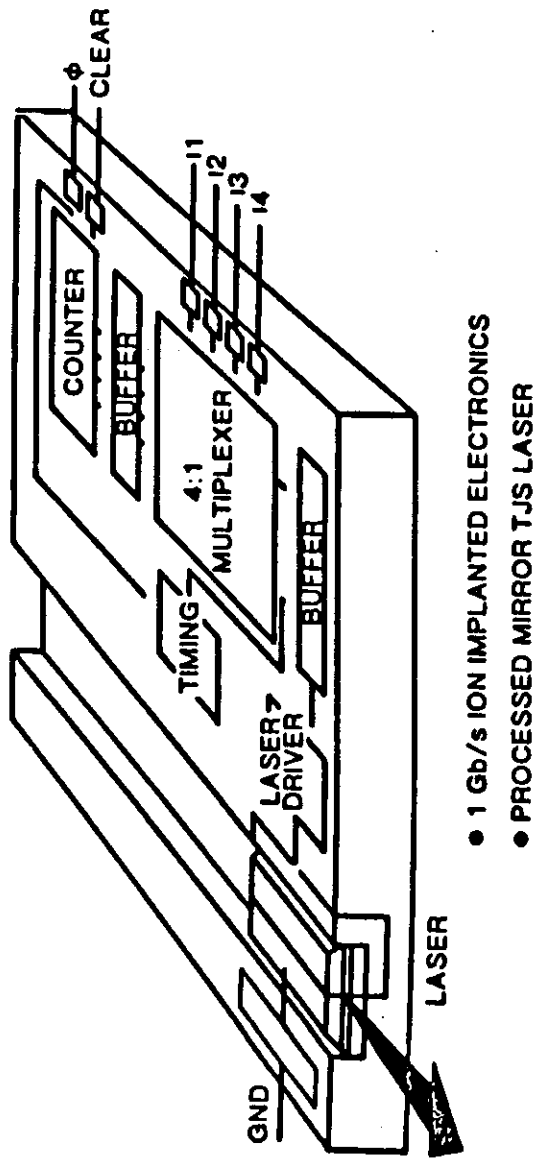

- 1 Gb/s ION IMPLANTED ELECTRONICS
- PROCESSED MIRROR TJS LASER

HITACHI MONOLITHIC AlGaAs/GaAs TRANSMITTER (LASER, PHOTODIODE AND FETs)

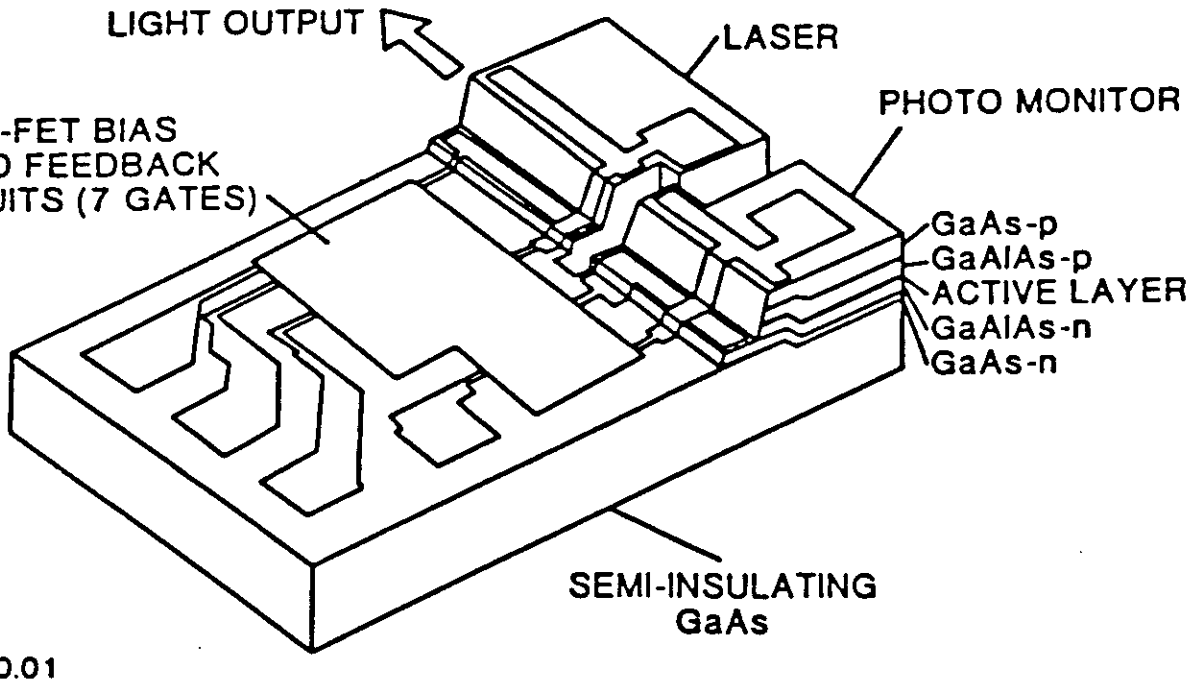

BCRM30.01